Supporting Information

Porous oligomeric materials synthesised using newly, highly active precatalyst based on ruthenium(III) and 2-phenylpyridine

*Kacper Pobłocki *[a], Katarzyna N. Jarzembska [b], Radosław Kamiński [b], Joanna Drzeżdżon [a], Krystyna A. Deresz [b], Dominik Schaniel [c], Anna Gołąbiewska [a], Barbara Gawdzik [d], Przemysław Rybiński [d], Dagmara Jacewicz *[a]*

[a]Department of Environmental Technology, Faculty of Chemistry, University of Gdansk, Wita Stwosza 63, 80-308 Gdansk, Poland.

[b]Department of Chemistry, University of Warsaw, Żwirki i Wigury 101, 02-089 Warsaw Poland.

[c.] Universite´ de Lorraine, CNRS, CRM2, F-54000 Nancy, France.

[d.]Institute of Chemistry, Jan Kochanowski University, Uniwersytecka 7, 25-406 Kielce, Poland.

Experimental

Materials

Almost all chemical compounds (except $RuCl_3NO$) were purchased from Merck, Darmstadt, Germany: 2-phenylpyridine (98% purity), toluene (99.5% purity), dimethyl sulfoxide (DMSO) (99.8% purity), hexane (99% purity), methylaluminoxane (MAO), ethylaluminium dichloride ($AlEtCl_2$), 2-propen-1-ol (98.5% purity), 2-chloro-2-propen-1-ol (90% purity), 3-buten-2-ol (97% purity), 2,3-dibromo-2-propen-1-ol (90% purity). $RuCl_3NO$ was purchased from BDH British Drug Houses, England (Fig. S29).

Complex compound synthesis

The **Ru1** compound is designed according to the principle of hard and soft Lewis acids and bases. **Ru1** was synthesized by adding 0.840 mL of 2-phenylpyridine (6 mmol) to 0.207 grams (1 mmol) of $RuCl_3NO$. Then 30 mL of H_2O/DMSO solution (v:v) was added to the flask and the mixture was heated for 2 hours under reflux until the solution turned scarlet. After one hour of heating, 20 mL of H_2O/DMSO (v:v) was added. After 14 days a single crystalline product was obtained.

Elemental analysis: C13H14O2N2RuCl2S; calculated: C 35.95%, H 3.25%, N 6.45%; found: C 36.11%, H 3.09%, N 6.29%.

Elemental analysis

Elemental analysis was carried out with an Elementar Vario EL III analyzer.

X-ray diffraction

Single-crystal X-ray measurement was performed on a Rigaku Oxford Diffraction SuperNova instrument equipped with a microfocus molybdenum X-ray source (Mo K_α radiation, λ = 0.71073 Å). During the measurement, a crystal was maintained at 100 K with the use of an Oxford Cryosystems nitrogen gas-flow device. Unit-cell parameter determination and raw diffraction image processing were performed with the native diffractometer *CRYSALISPRO* software suite. The structure was solved using an intrinsic phasing method as implemented in the *SHELXT* program[1] and refined with the *JANA* package [2] within the independent atom model approximation. The hydrogen atoms were placed geometrically with the riding model for the hydrogen thermal motion parameters applied (d_{C-H} = 0.96 Å, $U_{iso}^H = 1.2 \cdot U_{eq}^C$). The respective CIF files are available from the Supporting Information or can be retrieved from the Cambridge Structural Database[3,4] (deposition number: CCDC 2193867).

Spectroscopy

Almost all infrared (IR) measurements were performed using a Nicolet 5700 FTIR spectrometer (spectral resolution of 2 cm^{-1} in the range of 360–4000 cm^{-1}) equipped with a closed-cycle cryostat (Oxford Optistat V01). The sample was grinded, mixed with a spectroscopic-grade KBr, pressed into pellets, and glued to the cold finger of the cryostat using silver-paste thermal adhesive. During measurements, the sample was kept in a vacuum inside the cryostat. Irradiation of the sample was achieved through the cryostat window using various LEDs (Thorlabs L and LP series). IR spectra of oligomers were recorded ranging from

4000 to 400 cm^{-1} in KBr pellet (BRUKER IFS 66 spectrophotometer). Each spectrum consisted of 64 scans.

Computational analysis

All computations were carried out using the *GAUSSIAN* package (ver. 16) [5]. Molecule optimizations, isolated-molecule geometry optimizations, normal-mode frequencies and dimer interaction energies were calculated at the DFT(B3LYP)/6-311++G** level of theory [6–11]. For harmonic mode computations, no imaginary frequencies were found. In the case of interaction energy calculations, the Grimme empirical dispersion correction [10,11], modified by the Becke-Johnson damping function 34,35, and correction for basis set superposition error [14,15] were applied. The semi-automatic generation of input files was accomplished with the *CLUSTERGEN* program [16–18].

Oligomerization process

The oligomerization process of monomers was carried out in a glass vial with a silicon stopper to close off the air supply to the reaction mixture. First, 3 µmol of **Ru1** precatalyst were dissolved in a 2 mL mixture of toluene. The solution was then stirred for 15 minutes until the complex compound was completely dissolved. In the next step, an appropriate amount (optimization) of methylaluminoxane (MAO), which acted as an activator, and 3 mL of monomer (2-propen-1-ol/2-chloro-2-propen-1-ol/3-buten-2-ol/2,3-dibromo-2-propen-1-ol) were added. On the other hand, during ethylene oligomerization, the monomer was introduced from a cylinder at a pressure of 0.3/0.5/0.8 bar. All oligomerization reactions were carried out at atmospheric pressure, at 30°C, 50°C, or 70°C, under a nitrogen atmosphere. After completion of the oligomerization process, the resulting gels were washed with a mixture of hydrochloric acid and methanol (in a molar ratio of 1:1) to get rid of the precatalyst residue. The oligomeric material was dried to a constant weight, then weighed and physicochemical analyses were performed. MALDI-TOF-MS, TGA, DSC, FTIR, and SEM analyses were performed for the oligomerization reaction products in which the highest catalytic activity was obtained.
Identical tests were performed with ethylaluminum dichloride as an activator, using *n*-hexane as solvent (instead of MAO as activator and toluene as solvent). However, the resulting gels were completely decomposed after washing with a mixture of acid and methanol, so they were not subjected to further physicochemical analyses.

MALDI-TOF-MS

The MALDI-TOF-MS spectra were recorded on the Bruker Biflex III company, (Branch Überlingen, Germany). 2,5-Dihydroxybenzoic acid (DHB) was used as a matrix.

Thermal analysis (TG)

TG was performed on NETZSCH TG 209 instrument in an argon atmosphere temperature range from 0 to 1000°C. The mass of samples subjected to thermal analysis was about 5 mg.

Differential scanning calorimetry (DSC)

DSC studies were performed using the equipment from Mettler Toledo in the range from − 150 to 500°C with a heating rate of 10 °C·min^{-1} in the inert atmosphere. The sample for the DSC measurements was about 5 mg.

Scanning Electron Microscope (SEM)

The morphology of the prepared Ru1 and oligomers was investigated using a field-emission scanning electron microscope (SEM). For sample preparation, a certain amount of the powder was deposited onto carbon tape and was imaged with JEOL JSM-7610 F operating at 15 kV.

The BET and Langmuir surface area

The BET and Langmuir surface area study was determined using sorption analyzer 3P Instrument Micro 200 in data collecting of BET surface area, isotherm, pore size, and volume. Total pore volume was calculated at pressure p/p0 = 0.99. Pore size distribution was calculated using the Horvath-Kawazoe / Saito-Foley (HK/SF) method was calculated using the 3P-Instrument PAS program.

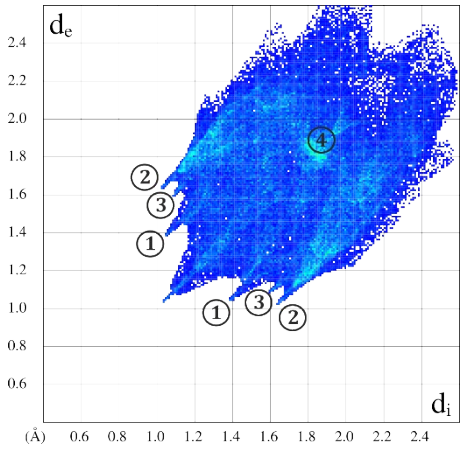

Figure S1. Hirshfeld fingerprint plot generated for the **Ru1** crystal structure; selected interatomic contact types are denoted with numbers: 1 – O···H, 2 – Cl···H, 3 – C···H, 4 – π···π.

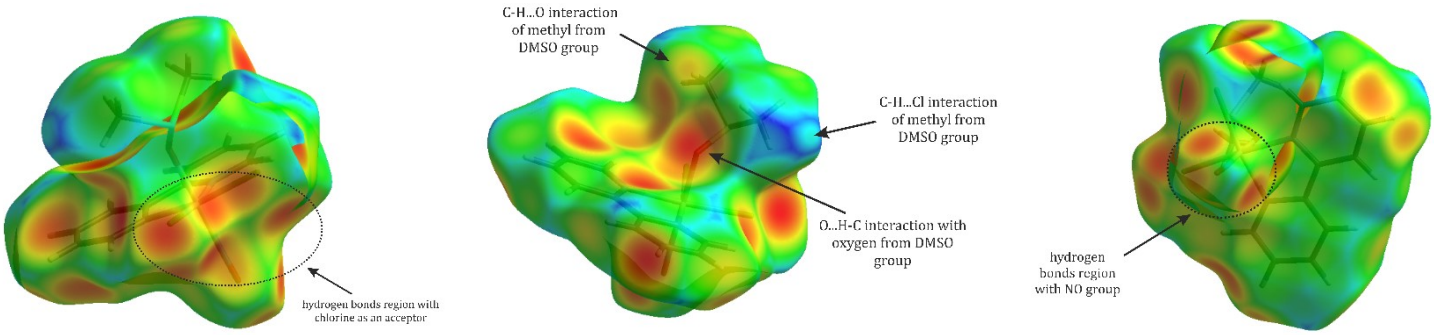

Figure S2. Hirshfeld surfaces with the d_e property mapped onto (1.03−2.69 Å range) illustrating hydrogen bonds in the analyzed crystal structure of **Ru1**.

Table S1. Reaction cavities determined for the NO and DMSO ligands based on selected structures retrieved from the Cambridge Structural Database (with *R*-factor < 5%), or from literature. In the case of the NO ligand, the cavities were calculated for structures known to be switchable under light irradiation.

REFCODE / Reference	*Ligand*	*Cavity volume,* V_{cav} / Å^3
Schaniel *et al.*[19]	NO	17.4
Mikhailov *et al.*[20]		23.6
CDMSOR10	O-bound DMSO	100.5
CDMSOR08		88.3
HALZUS		93.4
MEYZIC		109.2
CDMSOR10	S-bound DMSO	91.5
ATUNOU		115.3
CDMSOR08		95.6
HALZUS		96.1
MEYZIC		92.4

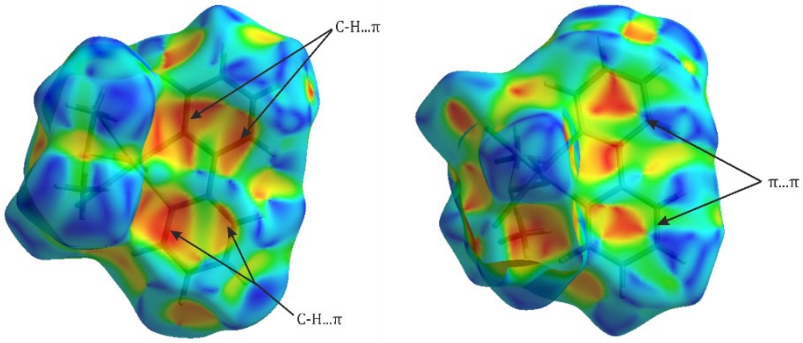

Figure S3. Shape index (from –1.0 to 1.0 a.u.) mapped onto the Hirshfeld surfaces which illustrates well C–H···π and π-stacking interactions in the analyzed crystal structure of **Ru1**.

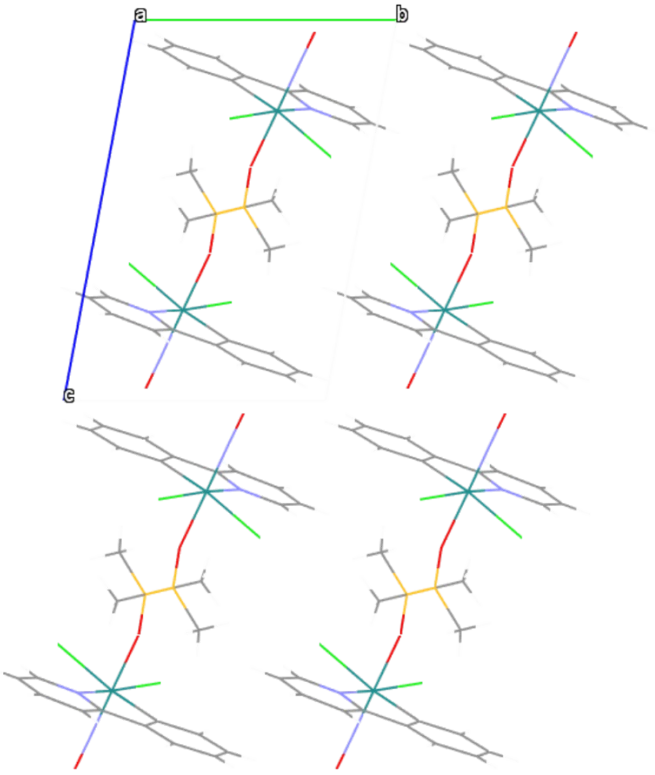

Figure S4. Crystal packing of **Ru1** (view along the *X*-axis).

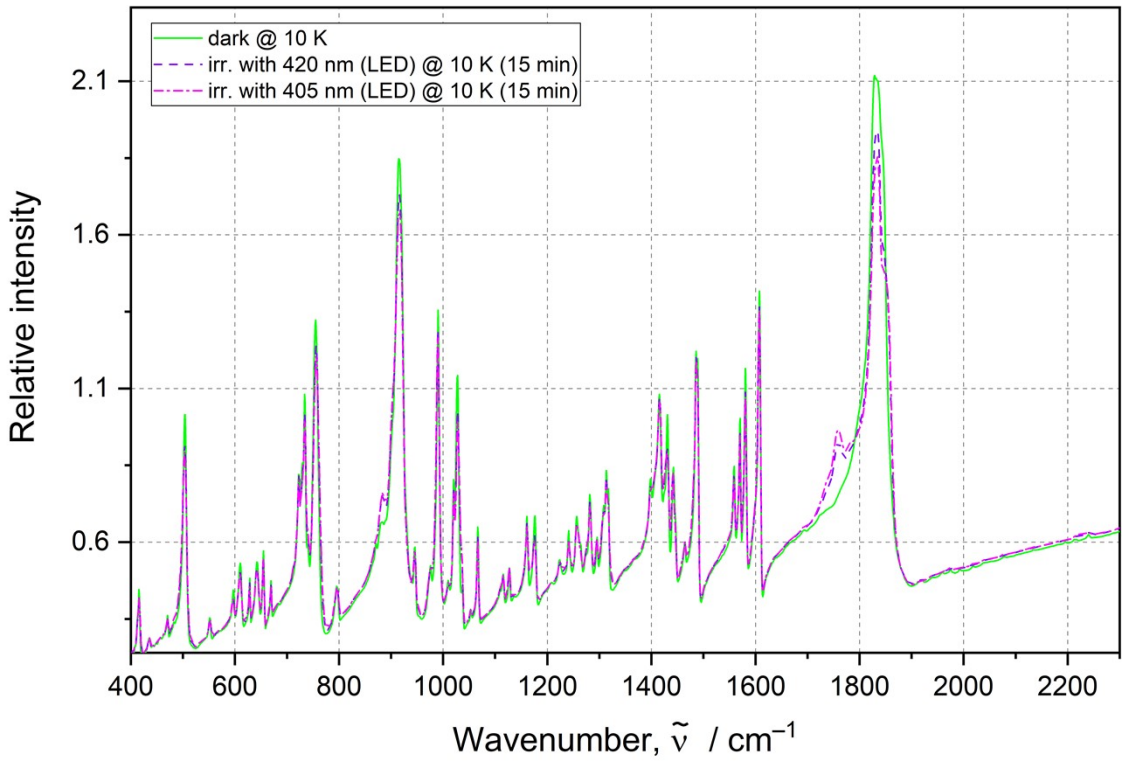

Figure S5. IR spectra collected at 10 K: no irradiation (green solid line), after irradiation with the 420 nm LED for 15 min. (violet dashed line), after irradiation with the 405 nm LED for 15 min. (magenta dashed-dotted line).

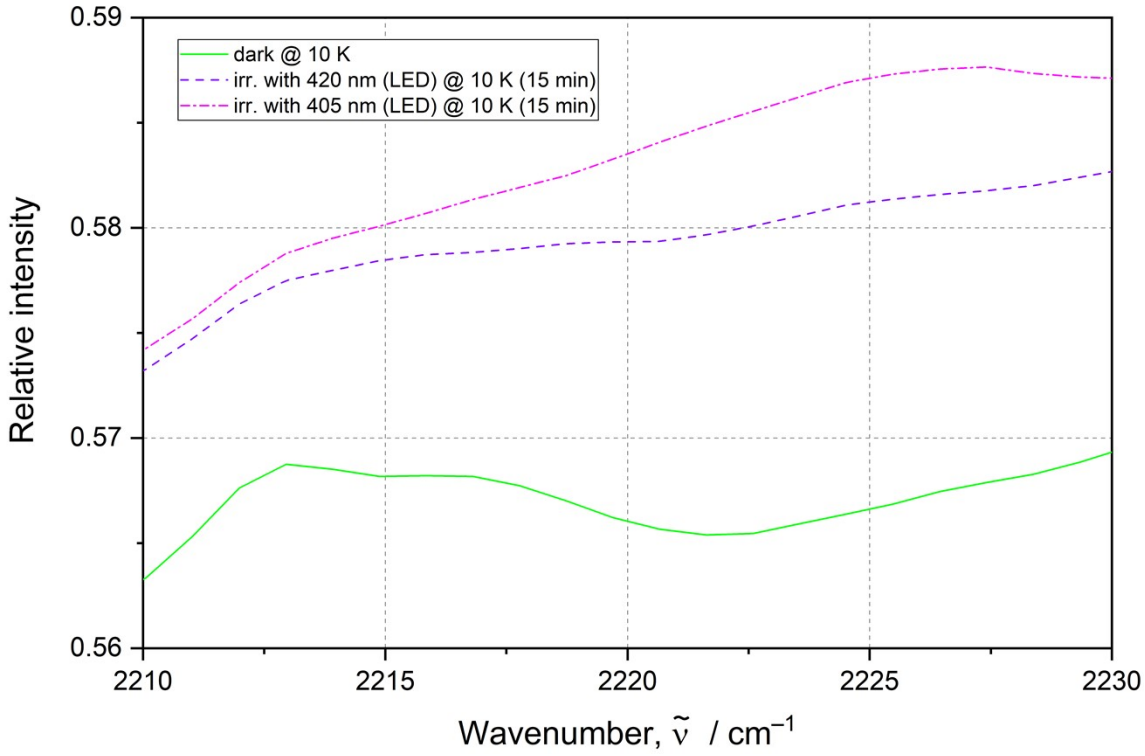

Figure S5 (continued). IR spectra collected at 10 K: no irradiation (green solid line), after irradiation with the 420 nm LED for 15 min. (violet dashed line), after irradiation with the 405 nm LED for 15 min. (magenta dashed-dotted line).

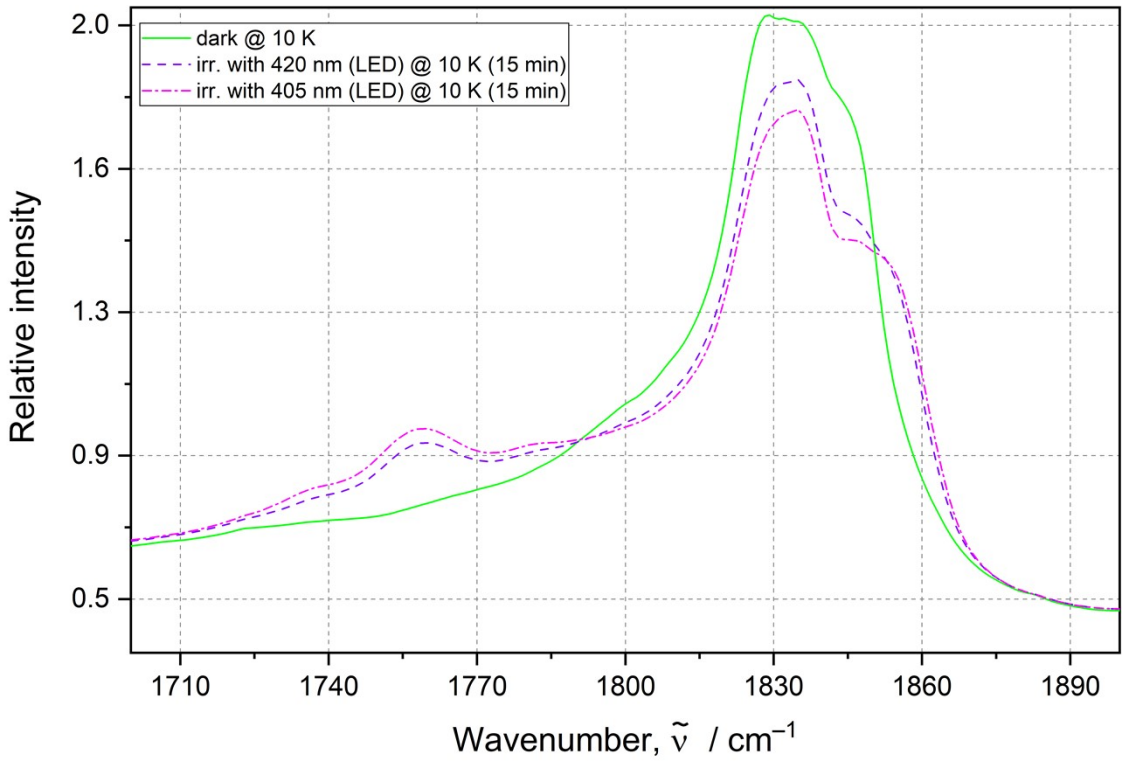

Figure S5 (continued). IR spectra collected at 10 K: no irradiation (green solid line), after irradiation with the 420 nm LED for 15 min. (violet dashed line), after irradiation with the 405 nm LED for 15 min. (magenta dashed-dotted line).

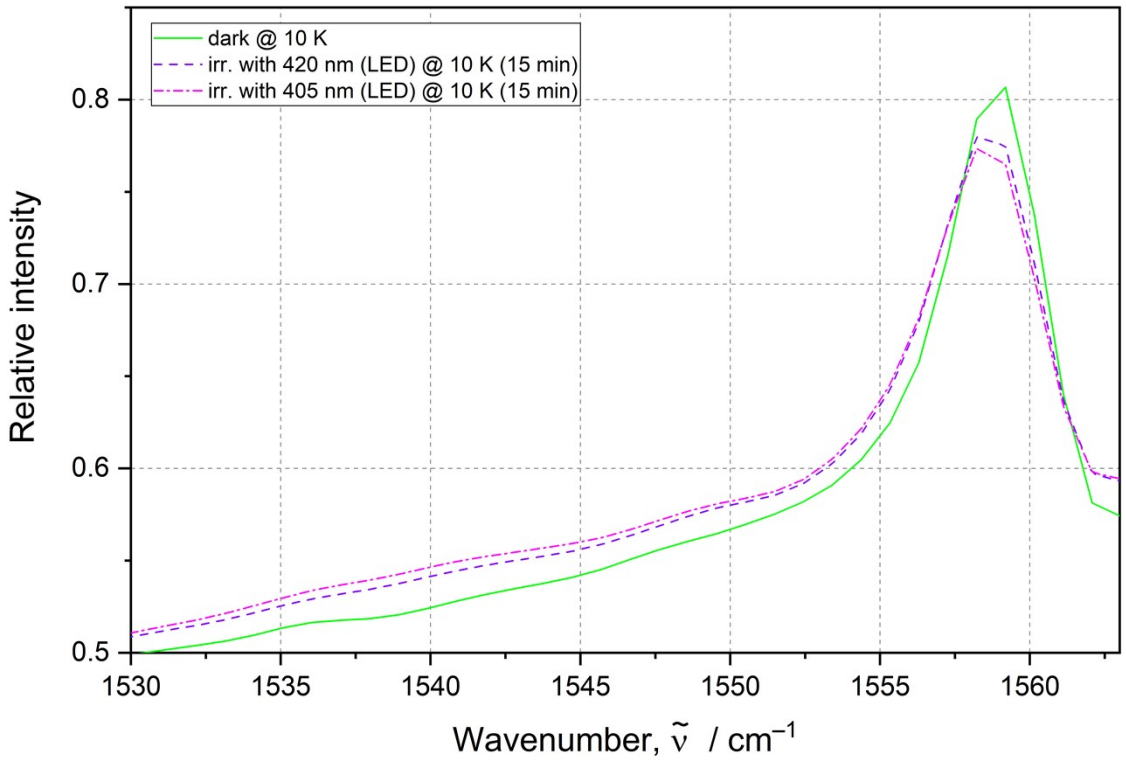

Figure S5 (continued). IR spectra collected at 10 K: no irradiation (green solid line), after irradiation with the 420 nm LED for 15 min. (violet dashed line), after irradiation with the 405 nm LED for 15 min. (magenta dashed-dotted line).

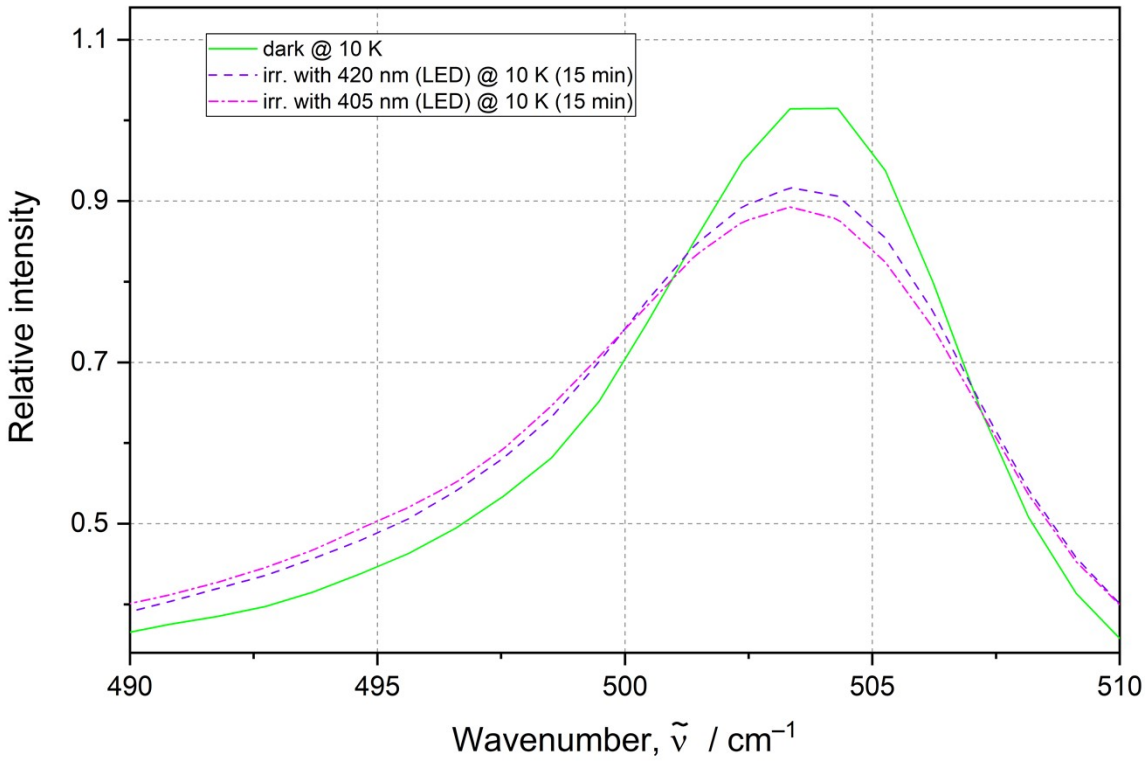

Figure S5 (continued). IR spectra collected at 10 K: no irradiation (green solid line), after irradiation with the 420 nm LED for 15 min. (violet dashed line), after irradiation with the 405 nm LED for 15 min. (magenta dashed-dotted line).

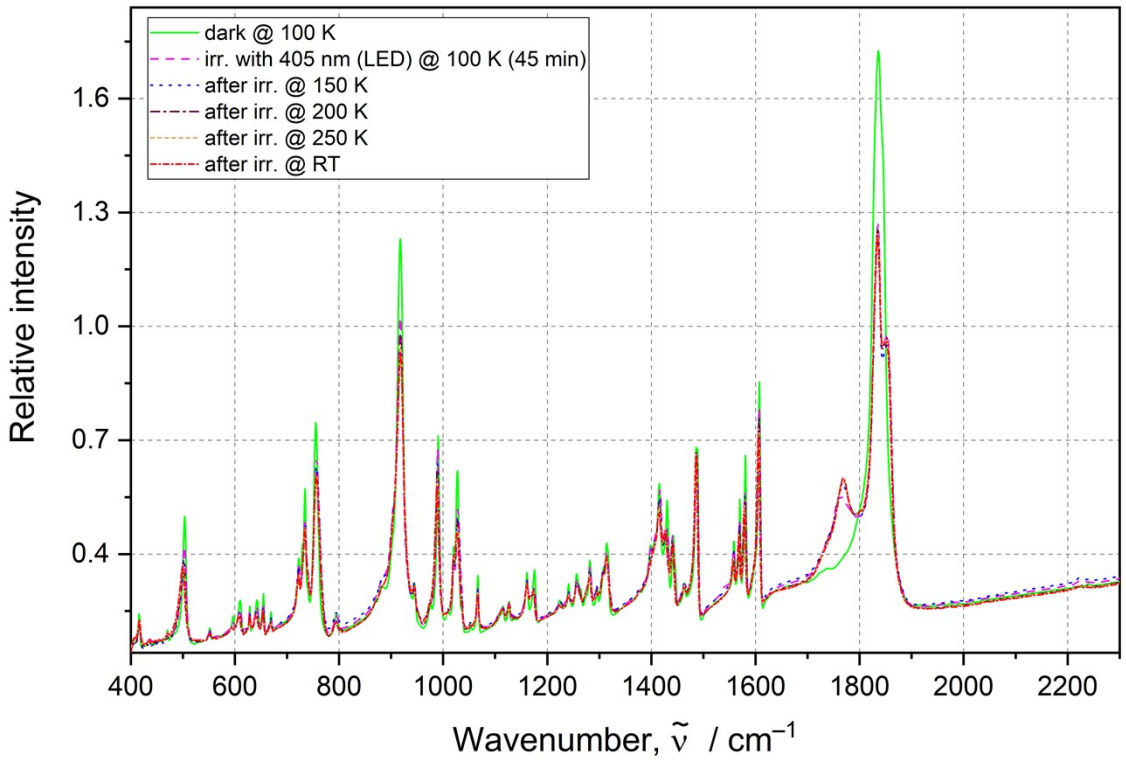

Figure S6. IR spectra collected at with no irradiation (green solid line) at 100 K, after irradiation with the 420 nm LED for 45 min. at 100 K (violet dashed line), and during temperature increasing: at 150 K (blue dotted line), at 200 K (brown dashed-dotted line), at 250 K (orange short dotted line) and at RT (red short dotted-dashed line).

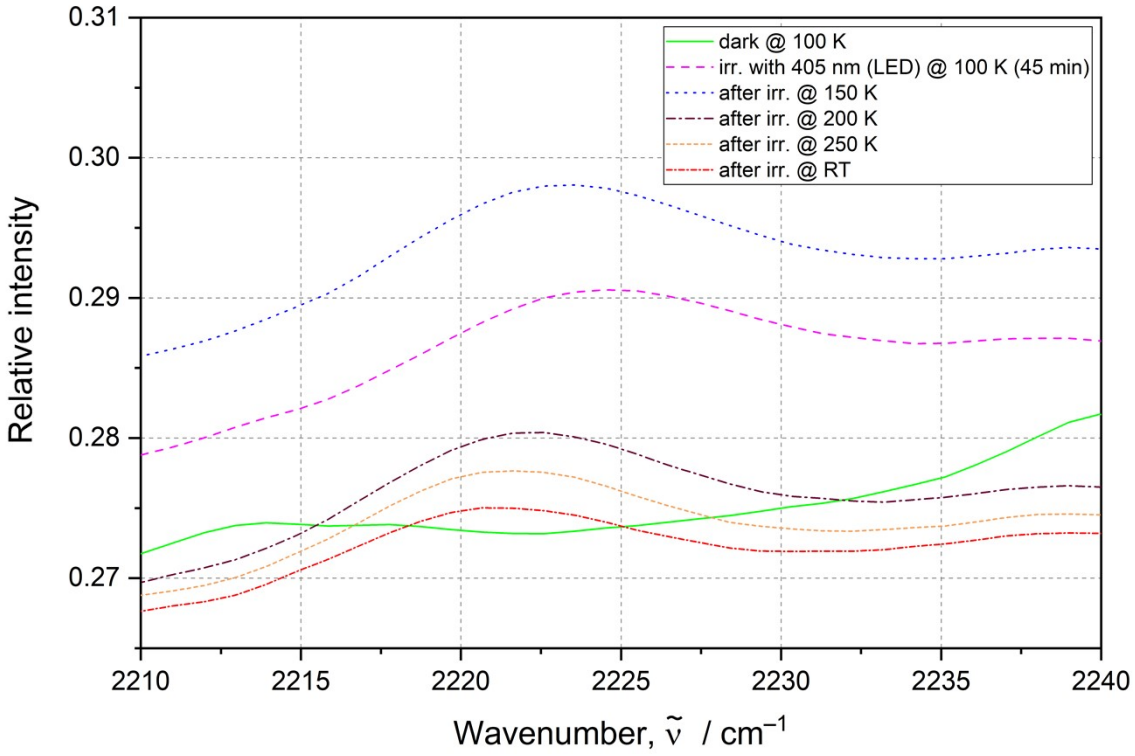

Figure S6 (continued). IR spectra collected at with no irradiation (green solid line) at 100 K, after irradiation with the 420 nm LED for 45 min. at 100 K (violet dashed line), and during temperature increasing: at 150 K (blue dotted line), at 200 K (brown dashed-dotted line), at 250 K (orange short dotted line) and at RT (red short dotted-dashed line).

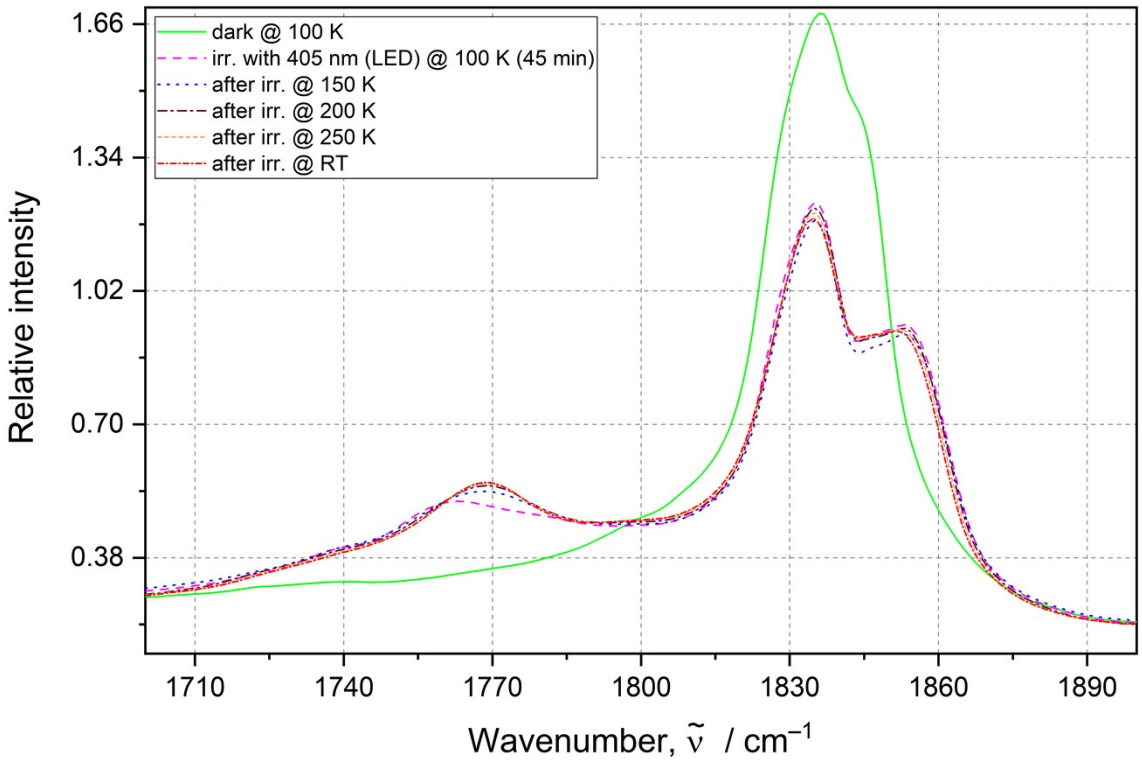

Figure S6 (continued). IR spectra collected at with no irradiation (green solid line) at 100 K, after irradiation with the 420 nm LED for 45 min. at 100 K (violet dashed line), and during temperature increasing: at 150 K (blue dotted line), at 200 K (brown dashed-dotted line), at 250 K (orange short dotted line) and at RT (red short dotted-dashed line).

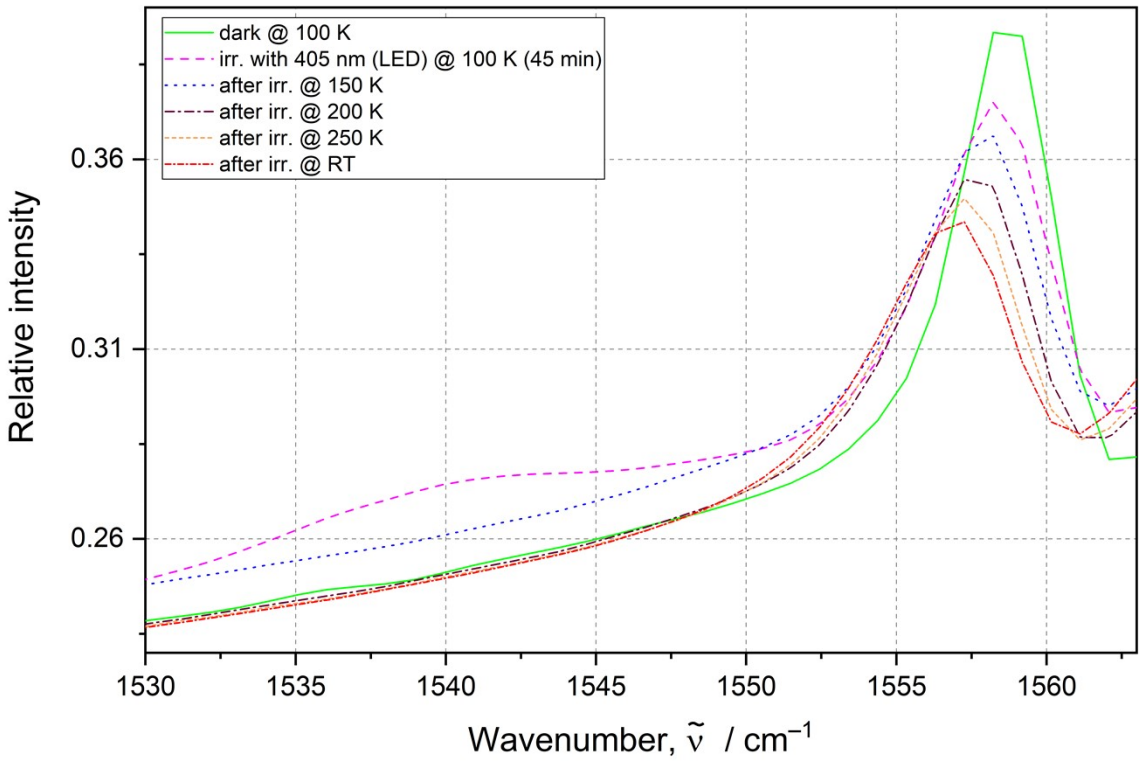

Figure S6 (continued). IR spectra collected at with no irradiation (green solid line) at 100 K, after irradiation with the 420 nm LED for 45 min. at 100 K (violet dashed line), and during temperature increasing: at 150 K (blue dotted line), at 200 K (brown dashed-dotted line), at 250 K (orange short dotted line) and at RT (red short dotted-dashed line).

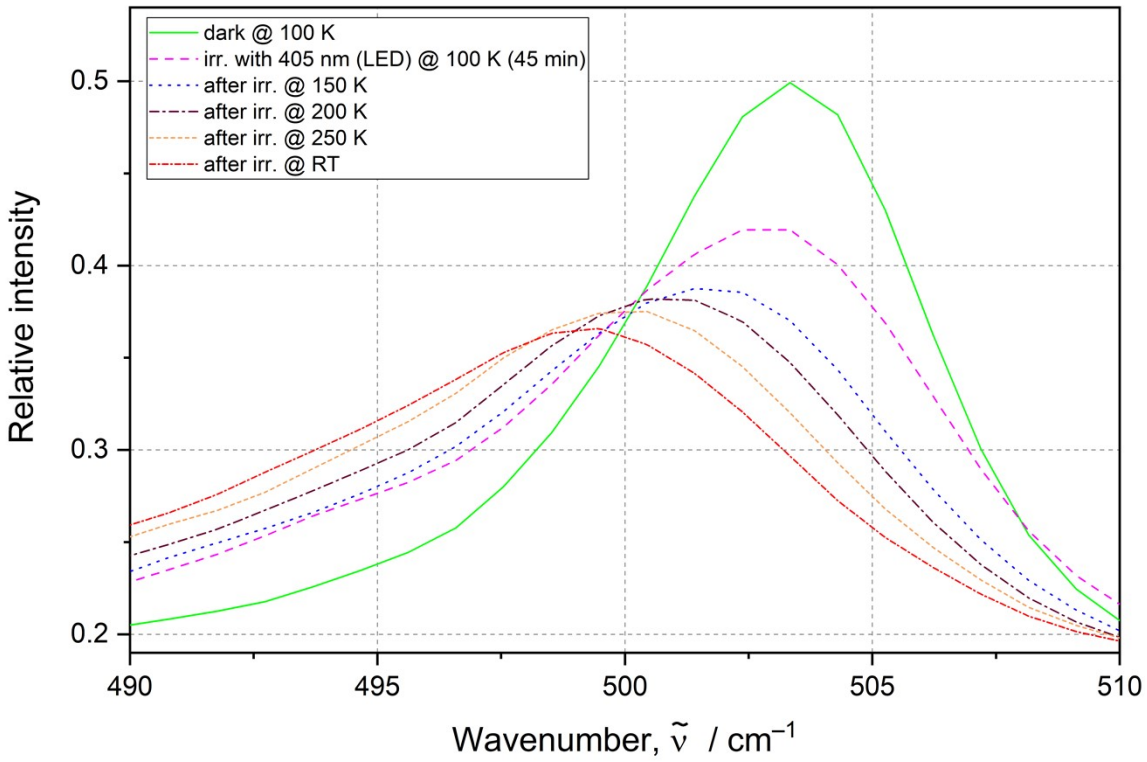

Figure S6 (continued). IR spectra collected at with no irradiation (green solid line) at 100 K, after irradiation with the 420 nm LED for 45 min. at 100 K (violet dashed line), and during temperature increasing: at 150 K (blue dotted line), at 200 K (brown dashed-dotted line), at 250 K (orange short dotted line) and at RT (red short dotted-dashed line).

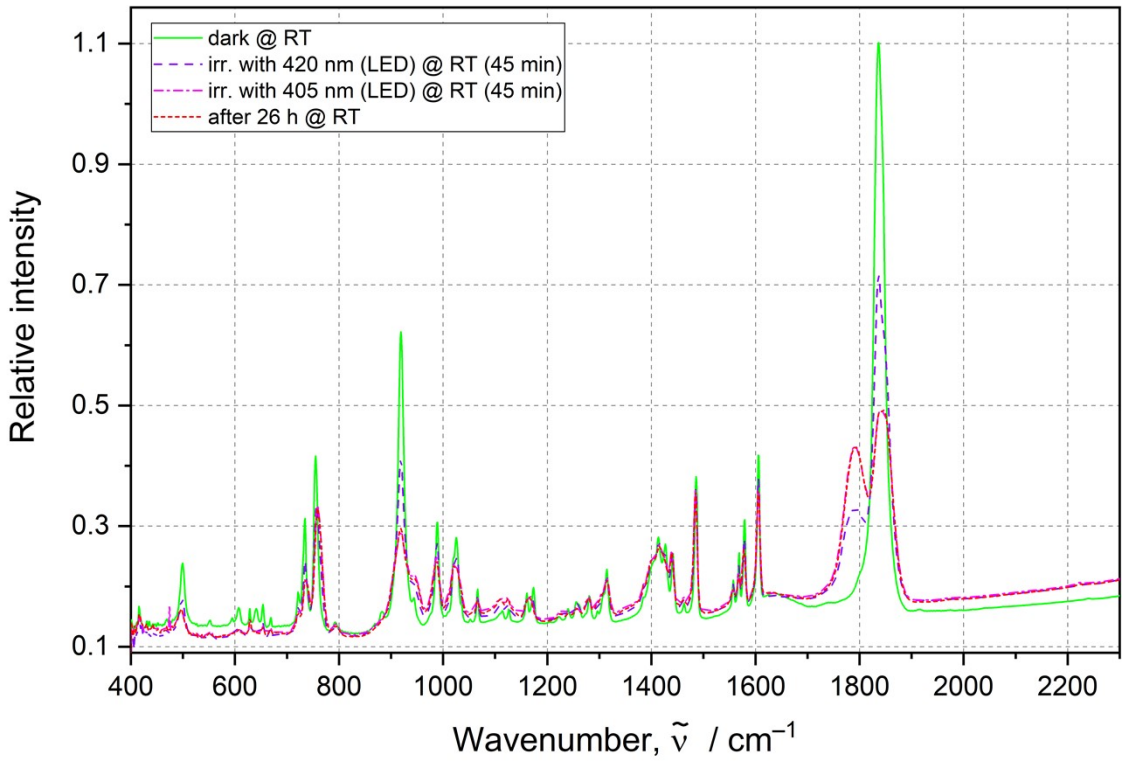

Figure S7. IR spectra collected at RT: no irradiation (green solid line), after irradiation with the 420 nm LED for 45 min. (violet dashed line), after irradiation with the 405 nm LED for 45 min. (magenta dashed-dotted line) and after subsequent waiting for 26 h (red short dashed line).

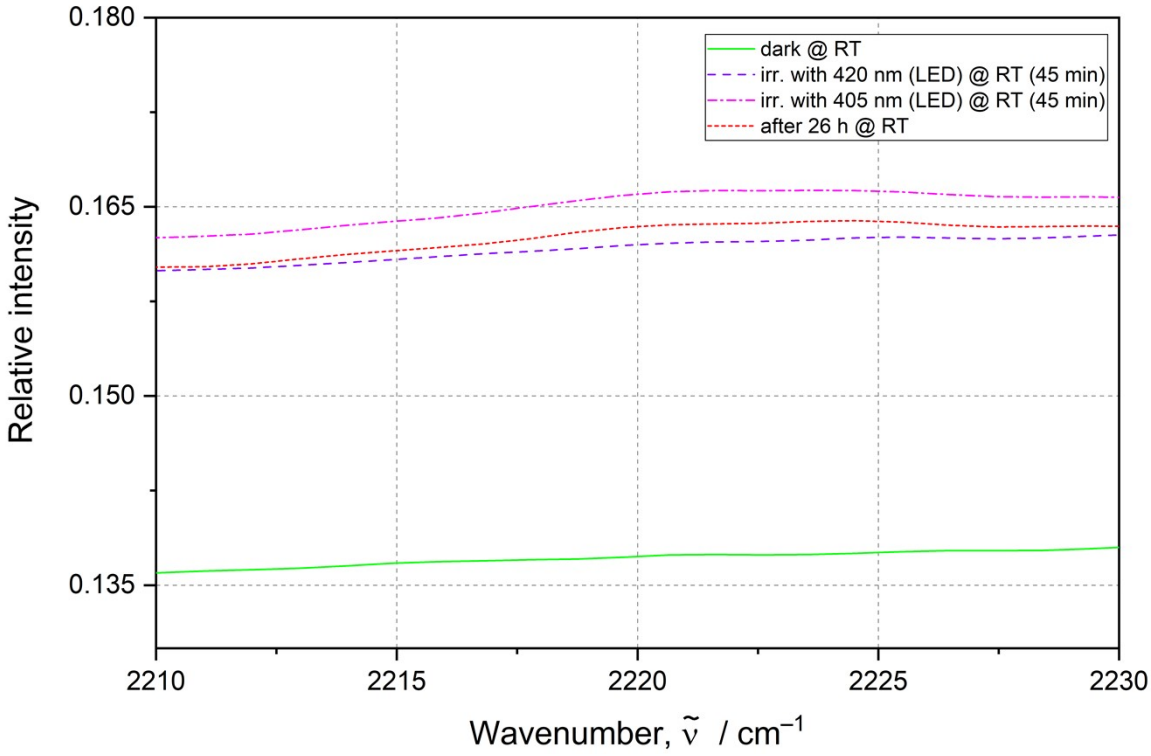

Figure S7 (continued). IR spectra collected at RT: no irradiation (green solid line), after irradiation with the 420 nm LED for 45 min. (violet dashed line), after irradiation with the 405 nm LED for 45 min. (magenta dashed-dotted line) and after subsequent waiting for 26 h (red short dashed line).

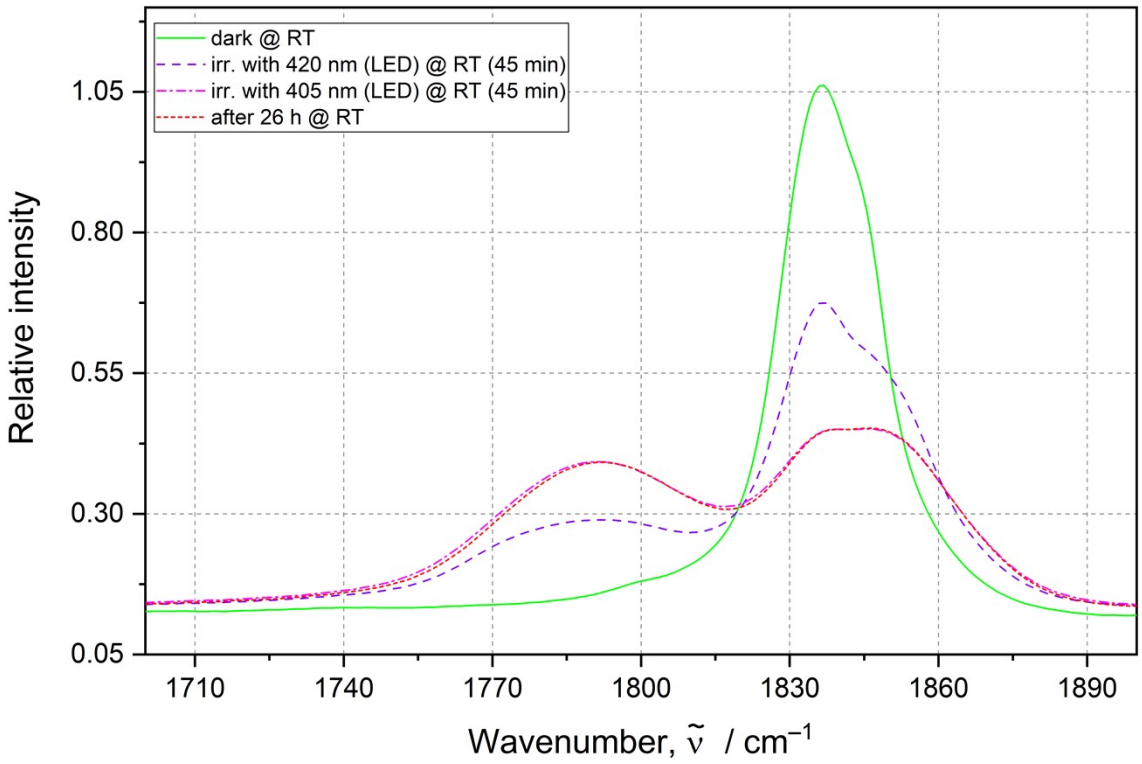

Figure S7 (continued). IR spectra collected at RT: no irradiation (green solid line), after irradiation with the 420 nm LED for 45 min. (violet dashed line), after irradiation with the 405 nm LED for 45 min. (magenta dashed-dotted line) and after subsequent waiting for 26 h (red short dashed line).

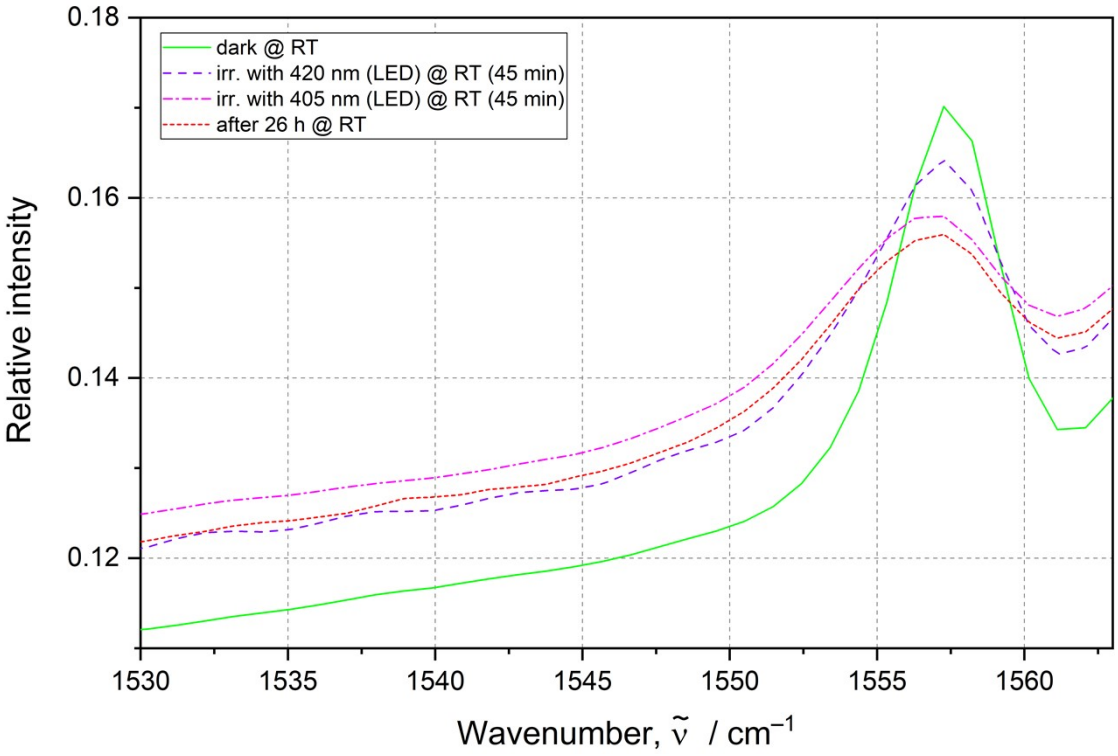

Figure S7 (continued). IR spectra collected at RT: no irradiation (green solid line), after irradiation with the 420 nm LED for 45 min. (violet dashed line), after irradiation with the 405 nm LED for 45 min. (magenta dashed-dotted line) and after subsequent waiting for 26 h (red short dashed line).

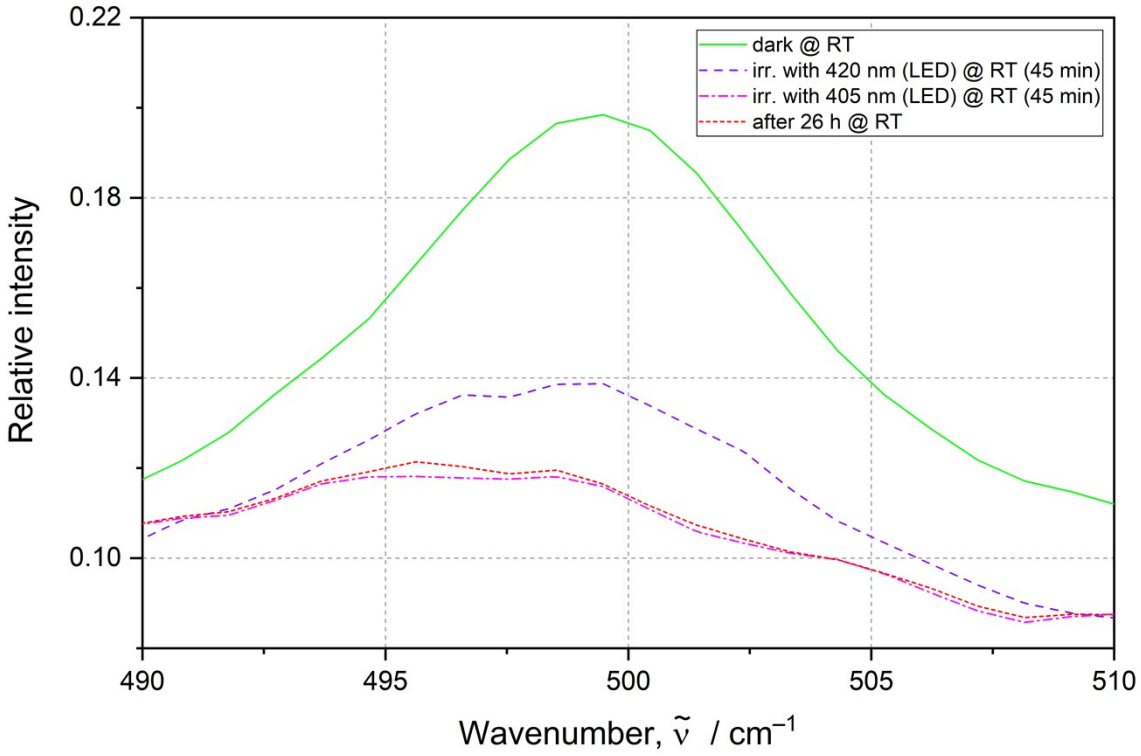

Figure S7 (continued). IR spectra collected at RT: no irradiation (green solid line), after irradiation with the 420 nm LED for 45 min. (violet dashed line), after irradiation with the 405 nm LED for 45 min. (magenta dashed-dotted line) and after subsequent waiting for 26 h (red short dashed line).

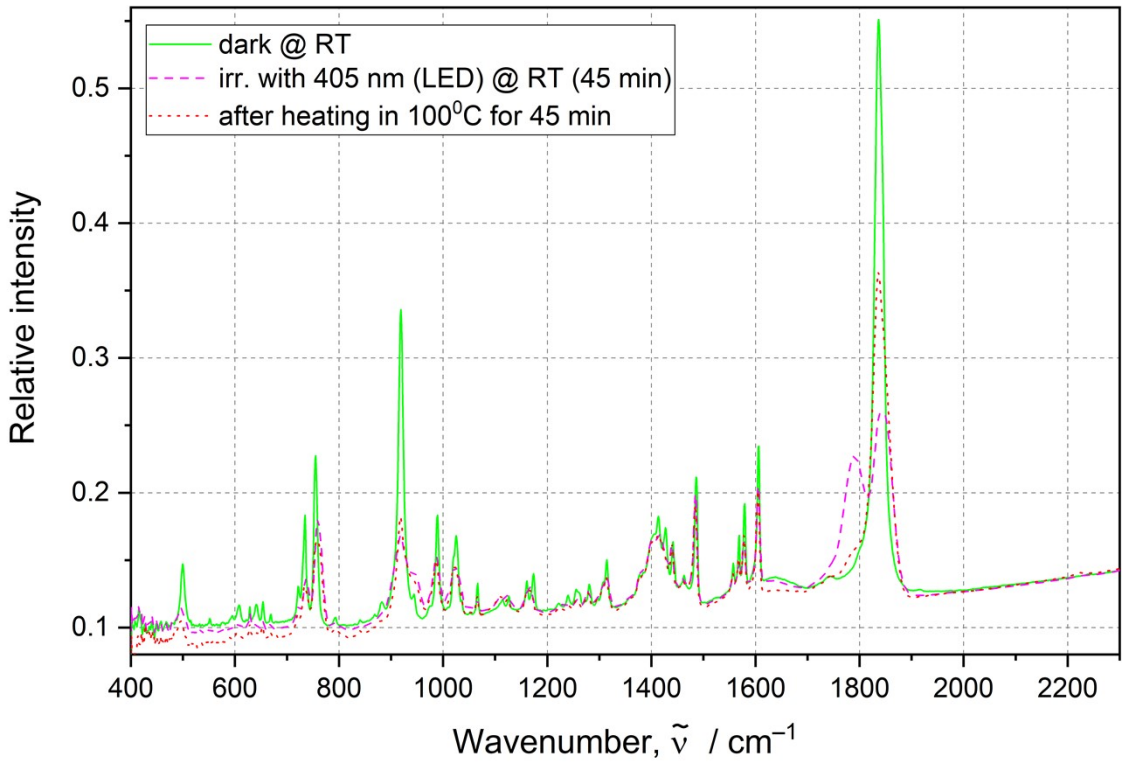

Figure S8. IR spectra collected at RT: no irradiation (green solid line), after irradiation with the 405 nm LED for 45 min. (magenta dashed line) and after heating in 100°C for 45 minutes (red short dashed line).

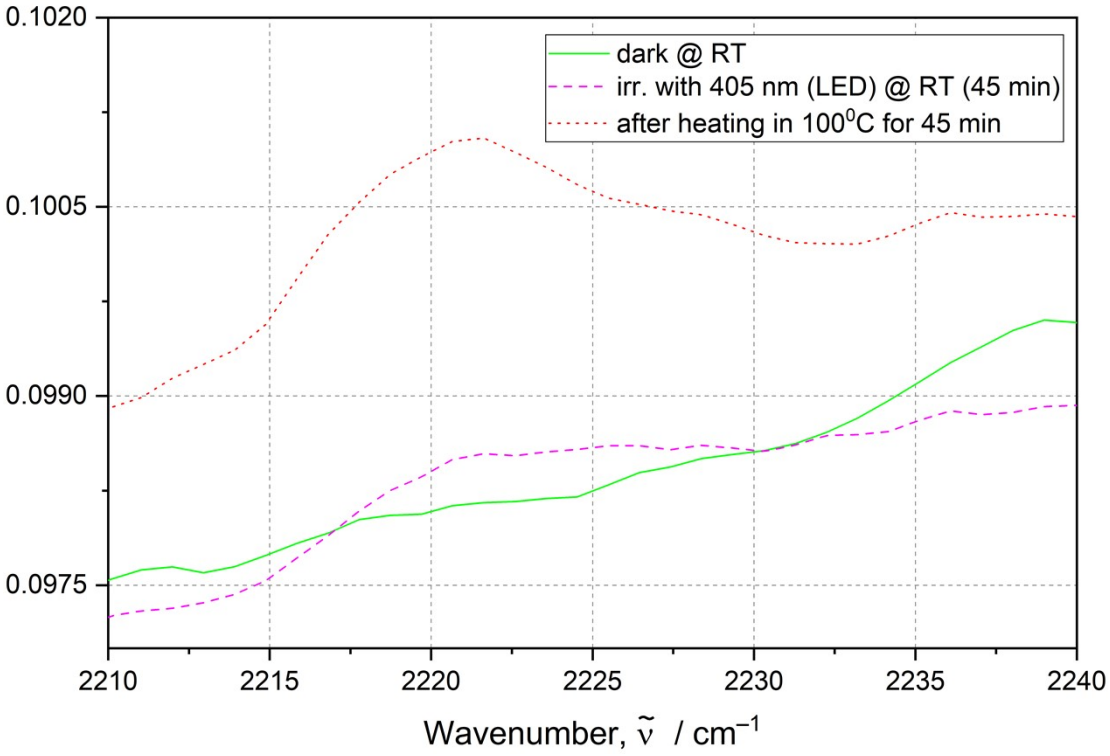

Figure S8 (continued). IR spectra collected at RT: no irradiation (green solid line), after irradiation with the 405 nm LED for 45 min. (magenta dashed line) and after heating in 100^{o}C for 45 minutes (red short dashed line).

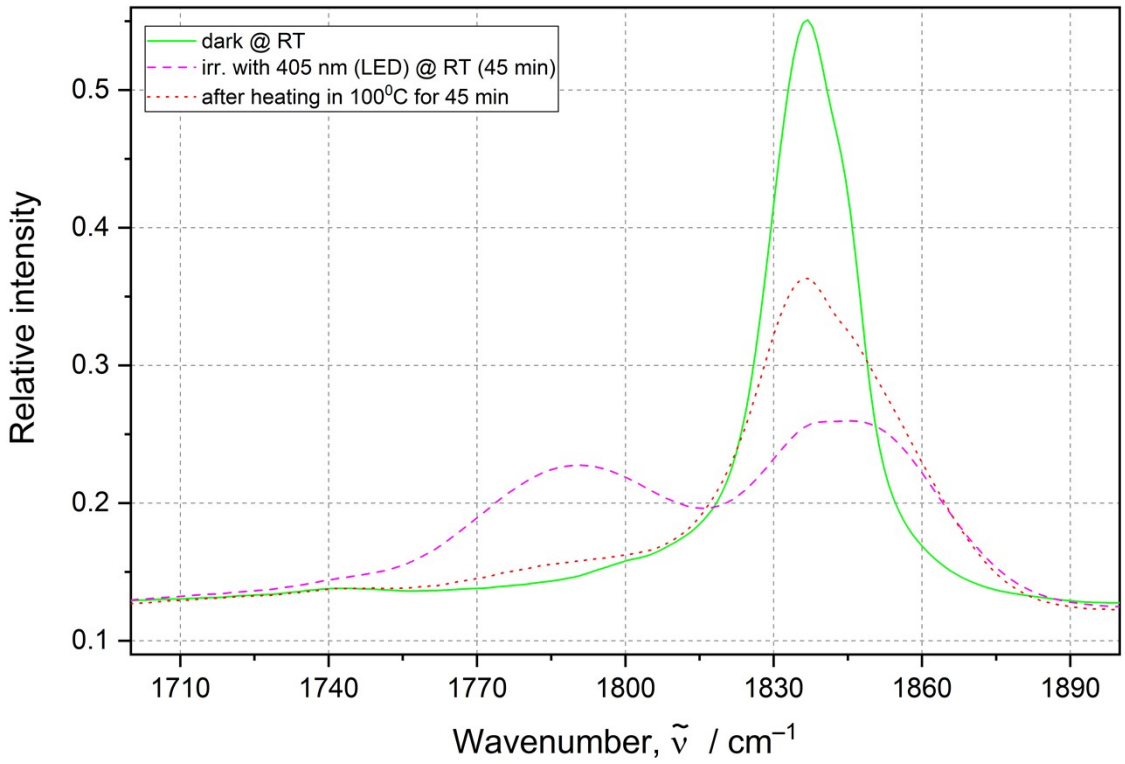

Figure S8 (continued). IR spectra collected at RT: no irradiation (green solid line), after irradiation with the 405 nm LED for 45 min. (magenta dashed line) and after heating in 100^{o}C for 45 minutes (red short dashed line).

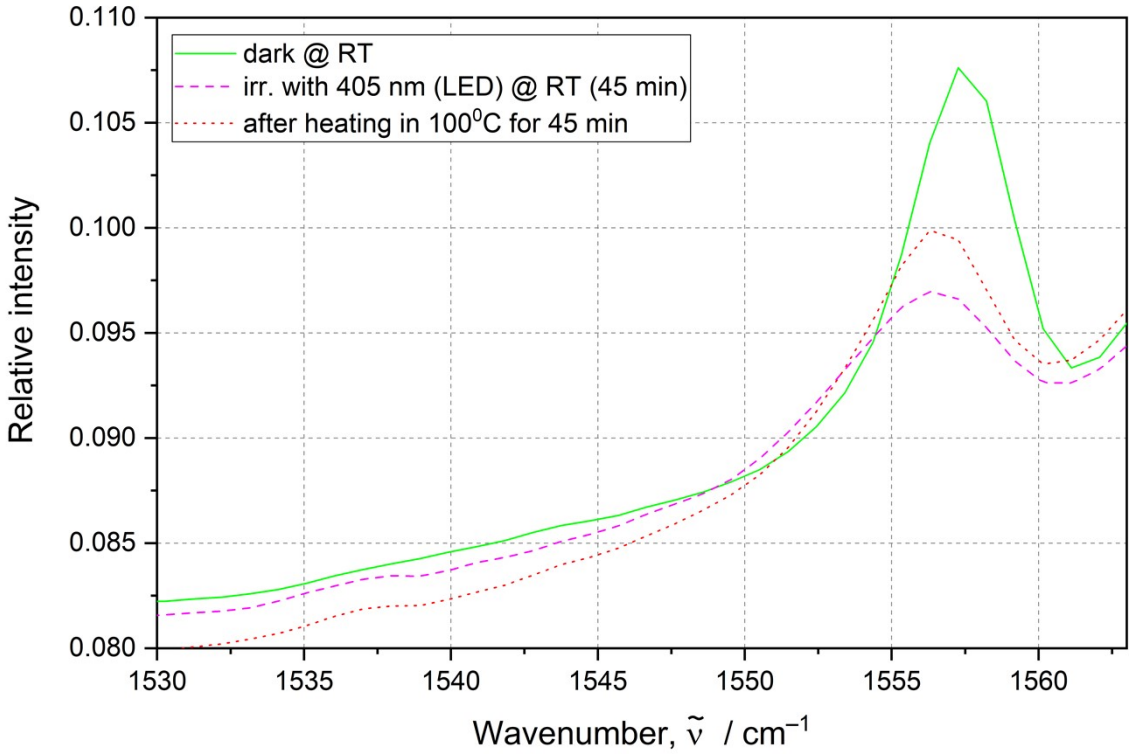

Figure S8 (continued). IR spectra collected at RT: no irradiation (green solid line), after irradiation with the 405 nm LED for 45 min. (magenta dashed line) and after heating in 100°C for 45 minutes (red short dashed line).

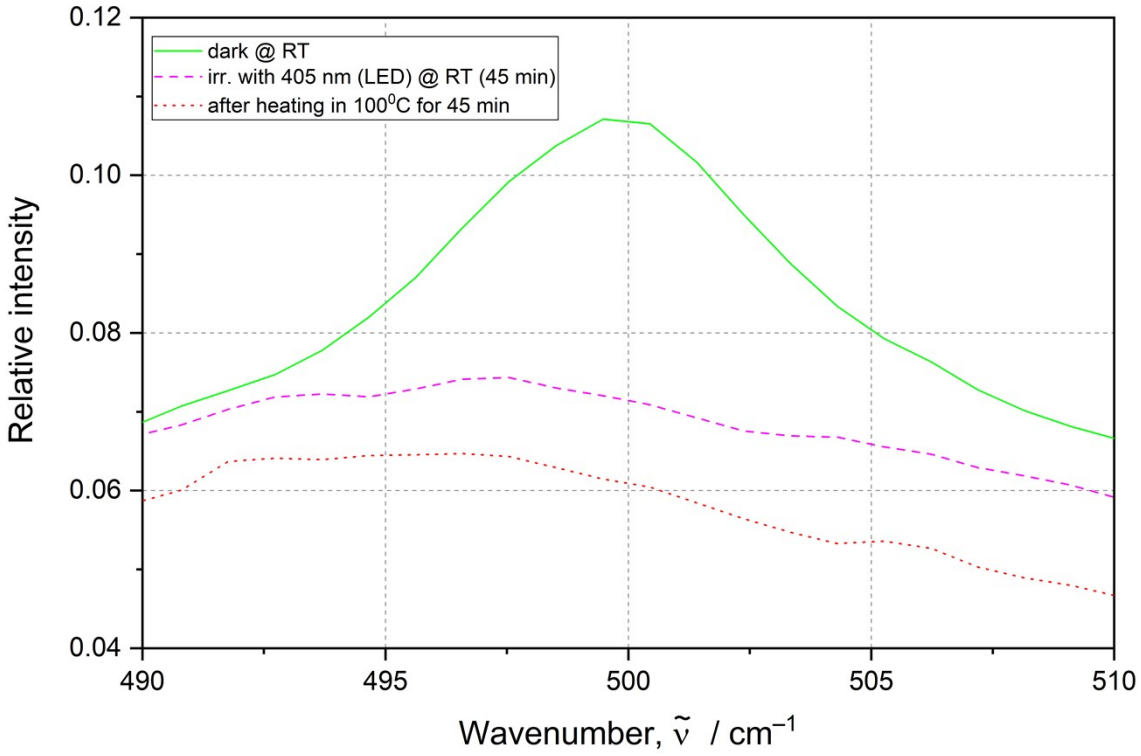

Figure S8 (continued). IR spectra collected at RT: no irradiation (green solid line), after irradiation with the 405 nm LED for 45 min. (magenta dashed line) and after heating in 100^{o}C for 45 minutes (red short dashed line).

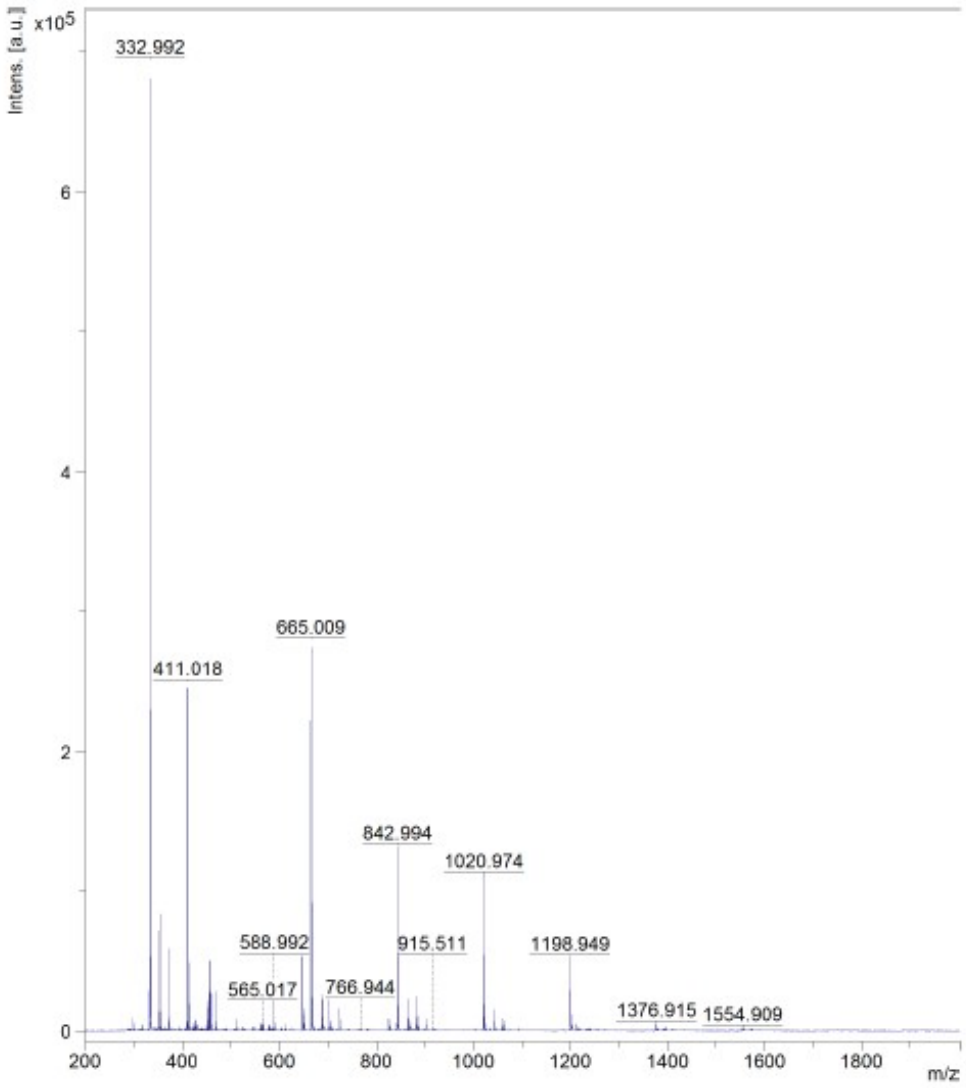

Figure S9. The MALDI-TOF-MS spectra of allyl alcohol oligomer.

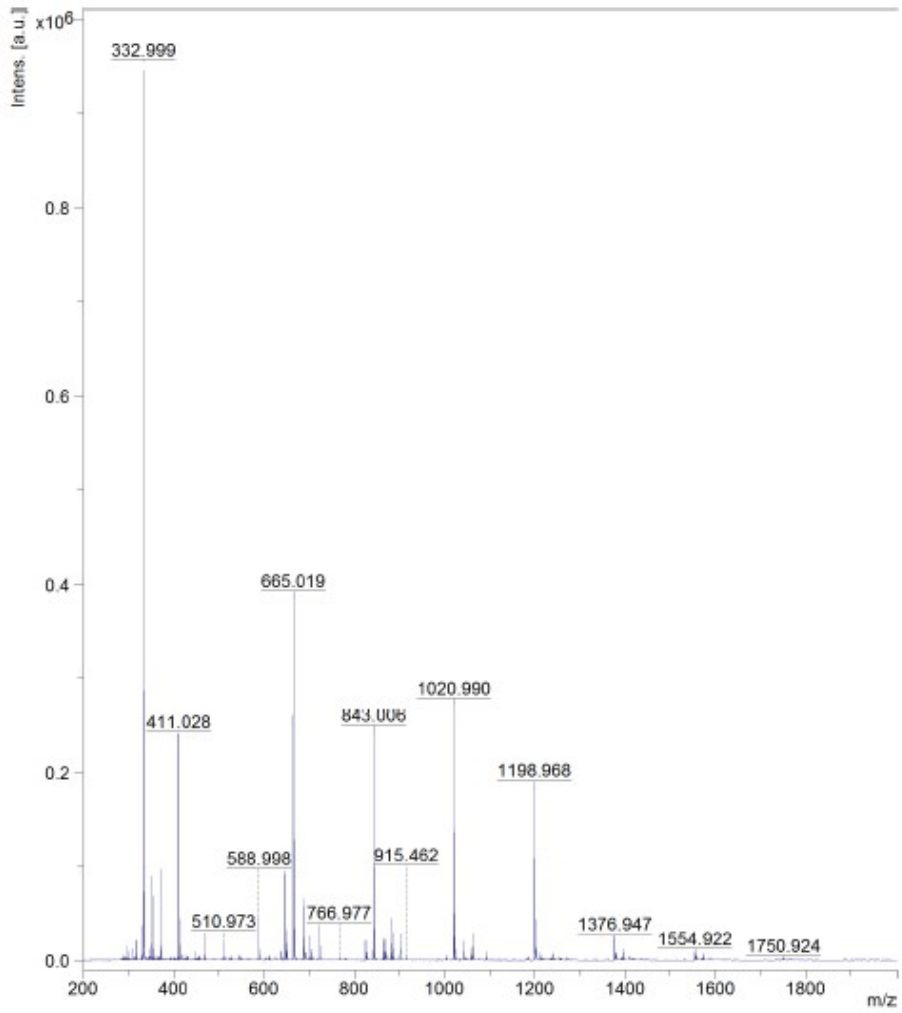

Figure S10. The MALDI-TOF-MS spectra of 2-chloro-2-propen-1-ol oligomer.

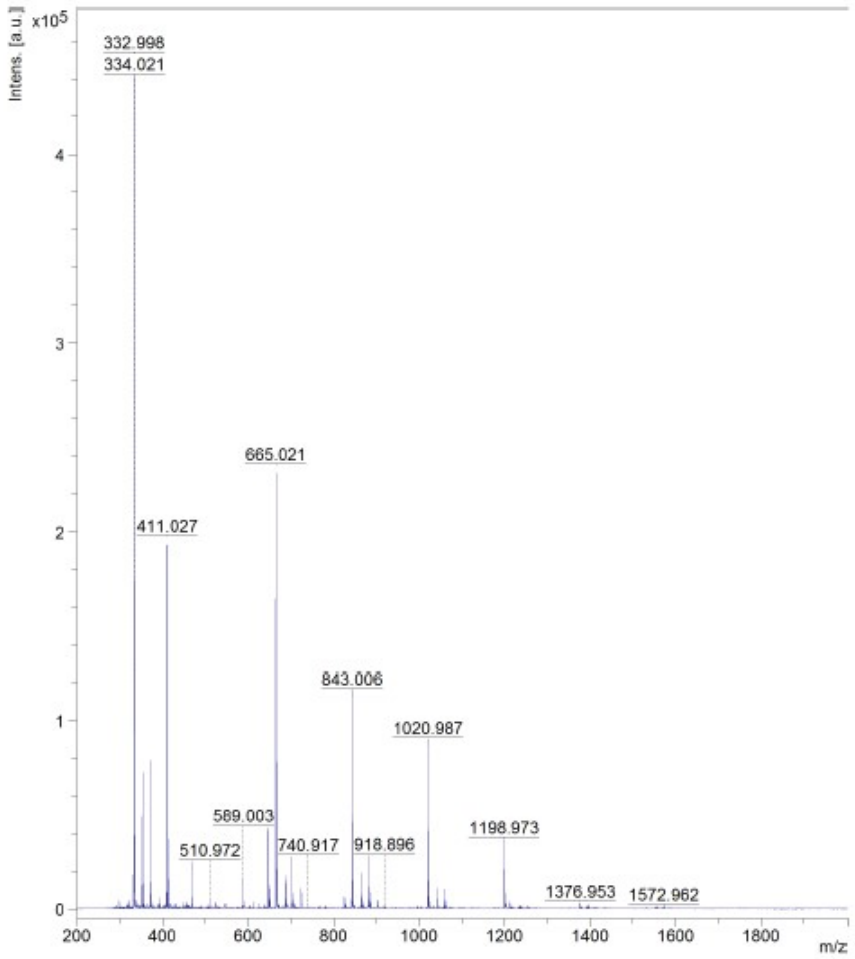

Figure S11. The MALDI-TOF-MS spectra of 3-buten-2-ol oligomer.

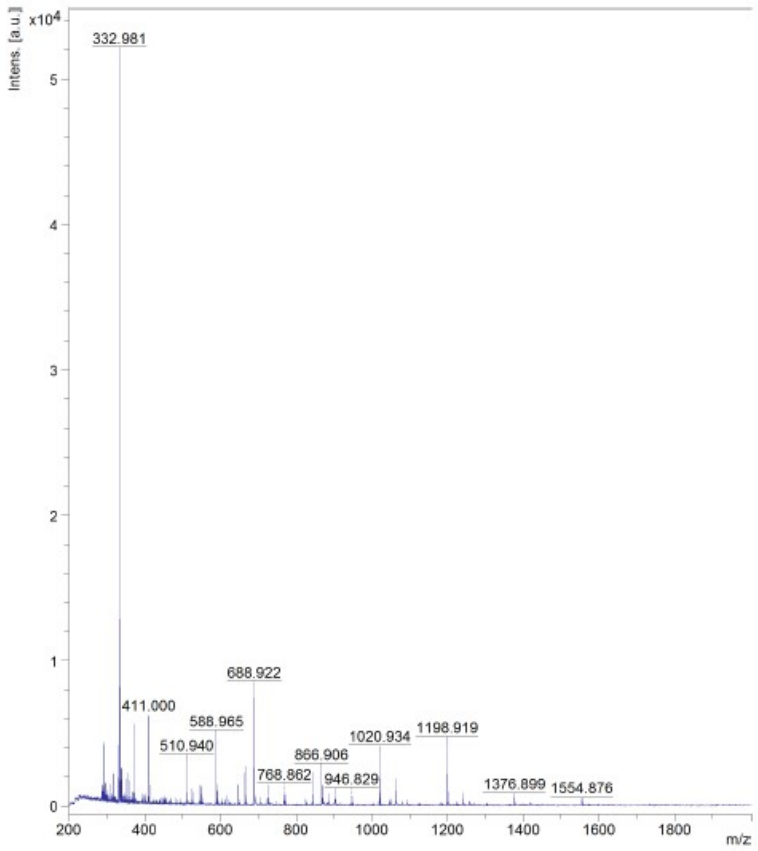

Figure S12. The MALDI-TOF-MS spectra of 2,3-dibormo-2-propen-1-ol oligomer.

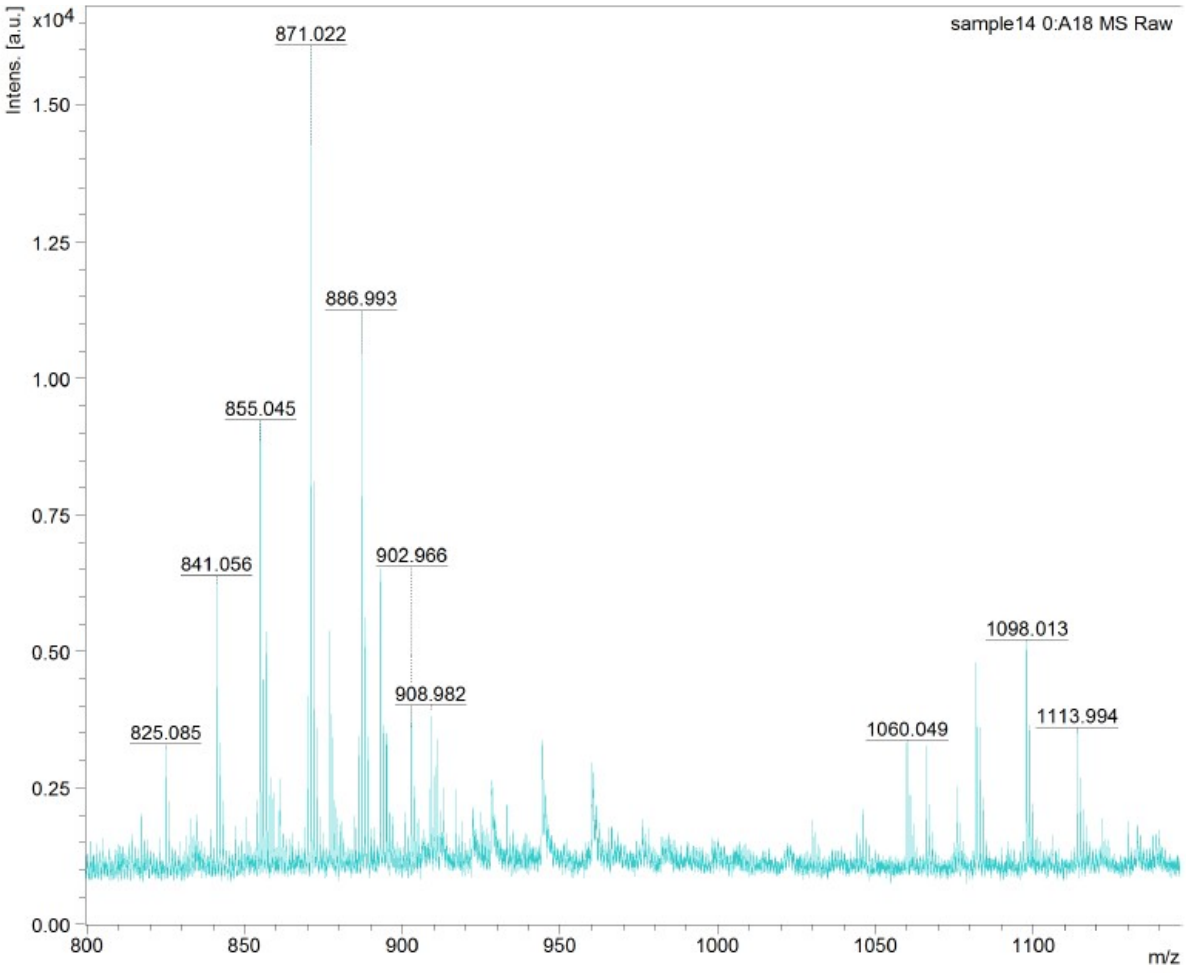

Figure S13. The MALDI-TOF-MS spectra of ethylene oligomer.

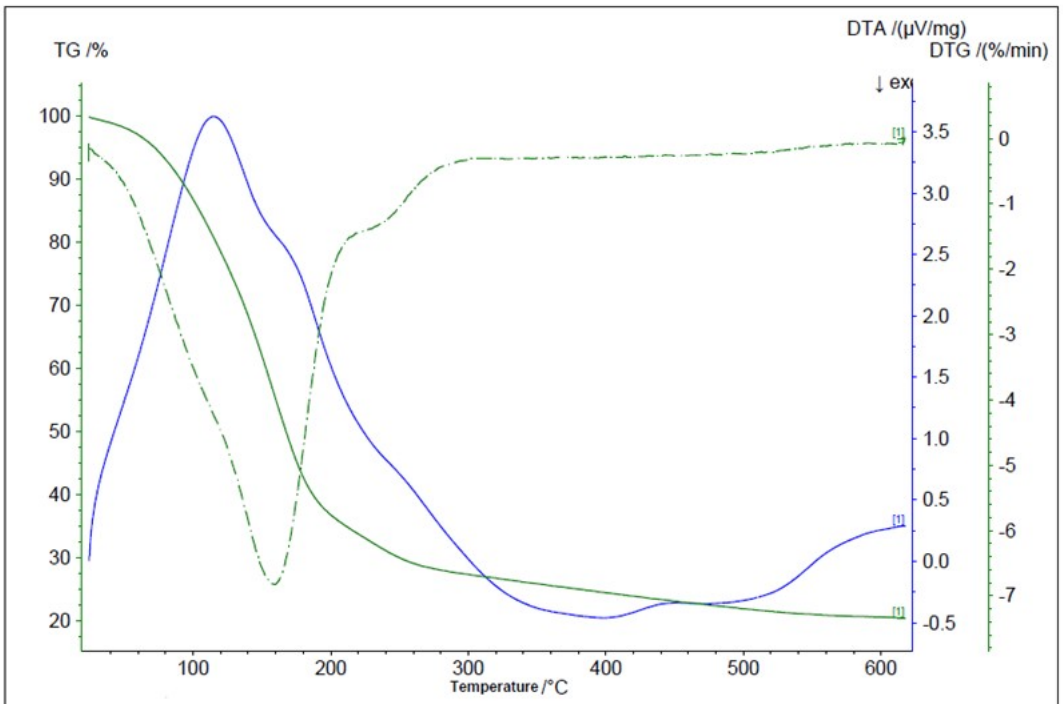

Figure S14. The TG and DTA curves for the allyl alcohol oligomer obtained using [Ru(2-phenylpyridine)$(Cl)_2$(DMSO)(NO)] as a precatalyst.

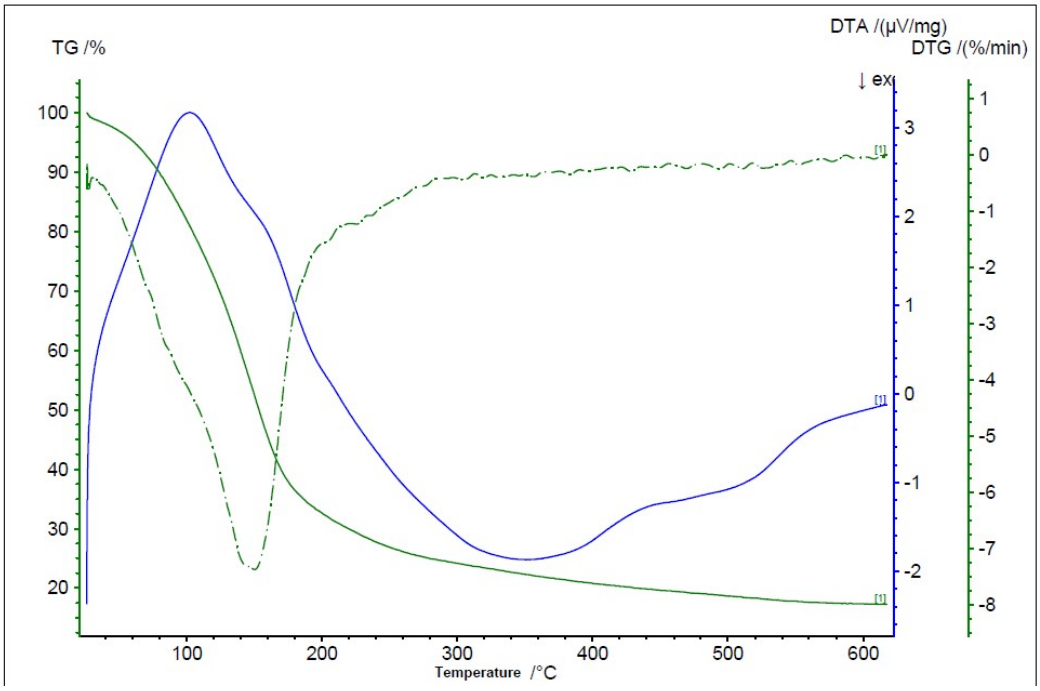

Figure S15. The TG and DTA curves for the 2-chloro-2-propen-1-ol oligomer obtained using [Ru(2-phenylpyridine)$(Cl)_2$(DMSO)(NO)] as a precatalyst.

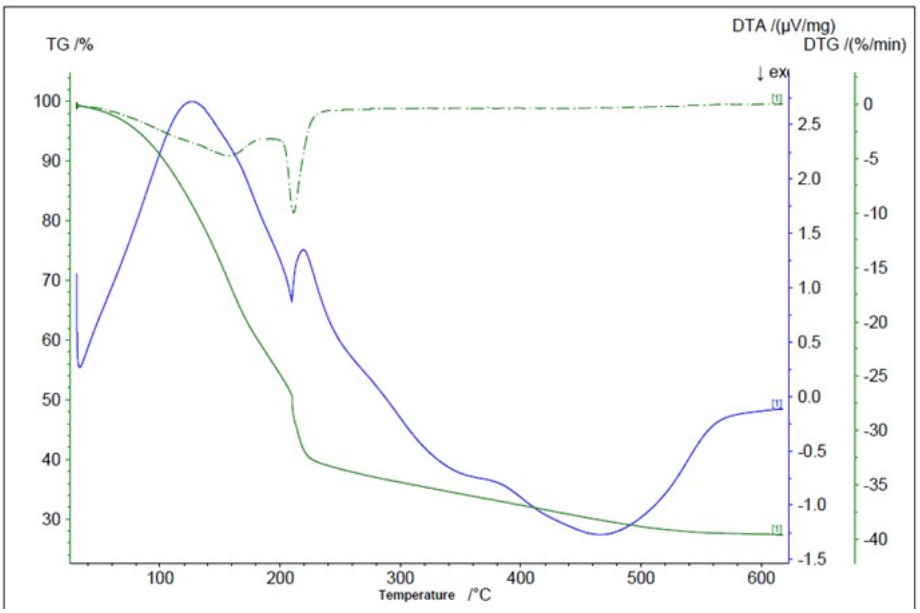

Figure S16. The TG and DTA curves for the 3-buten-2-ol oligomer obtained using [Ru(2-phenylpyridine)$(Cl)_2$(DMSO)(NO)] as a precatalyst.

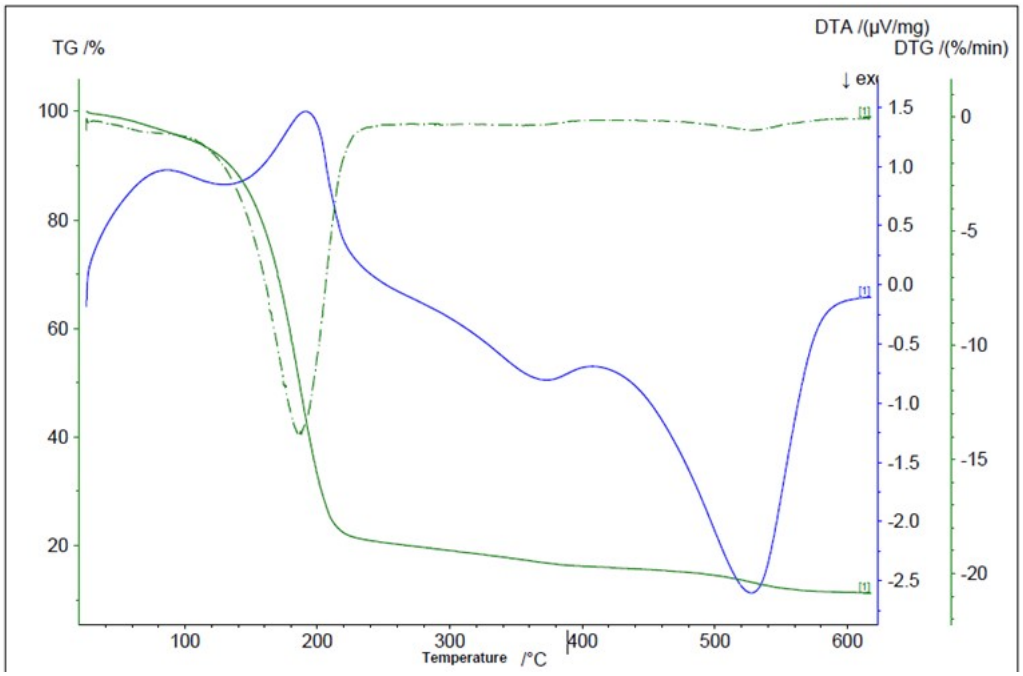

Figure S17. The TG and DTA curves for the 2,3-dibromo-2-propen-1ol oligomer obtained using [Ru(2-phenylpyridine)$(Cl)_2$(DMSO)(NO)] as a precatalyst.

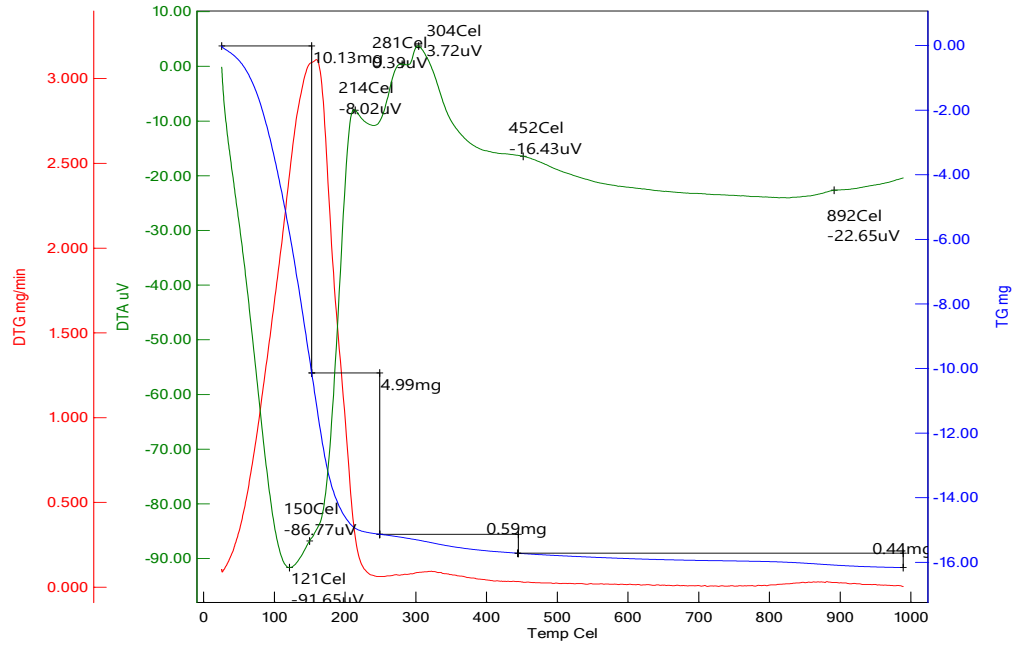

Figure S18. The TG and DTA curves for the ethylene oligomer obtained using [Ru(2-phenylpyridine)$(Cl)_2$(DMSO)(NO)] as a precatalyst.

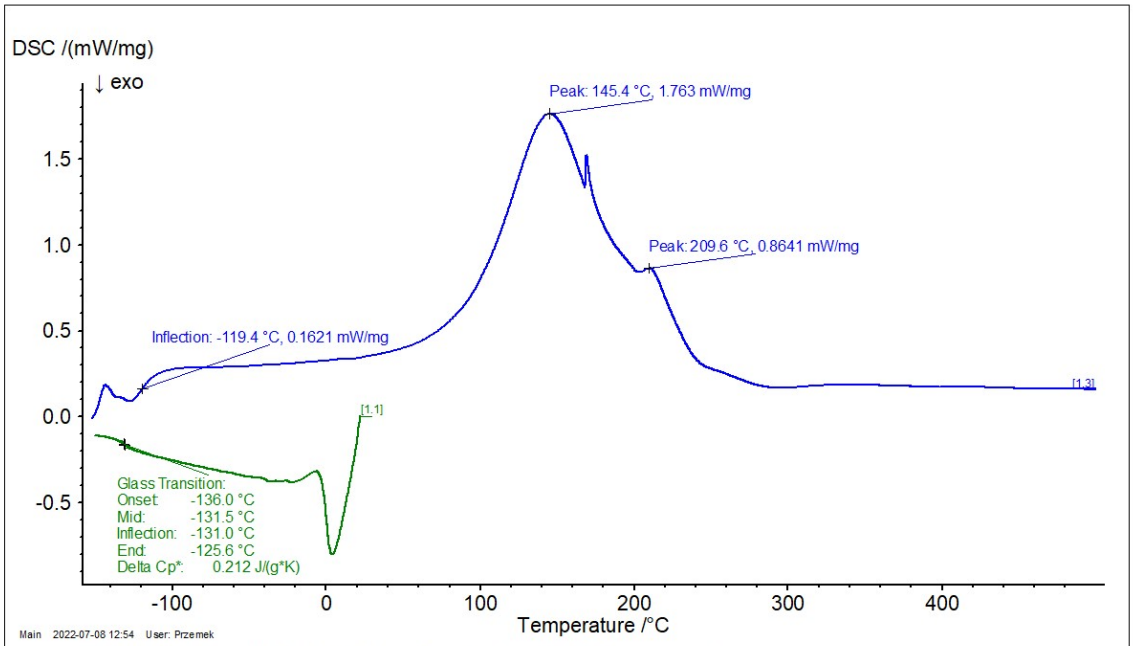

Figure S19. The DSC curve of allyl alcohol oligomer obtained using [Ru(2-phenylpyridine)$(Cl)_2$(DMSO)(NO)] as a precatalyst.

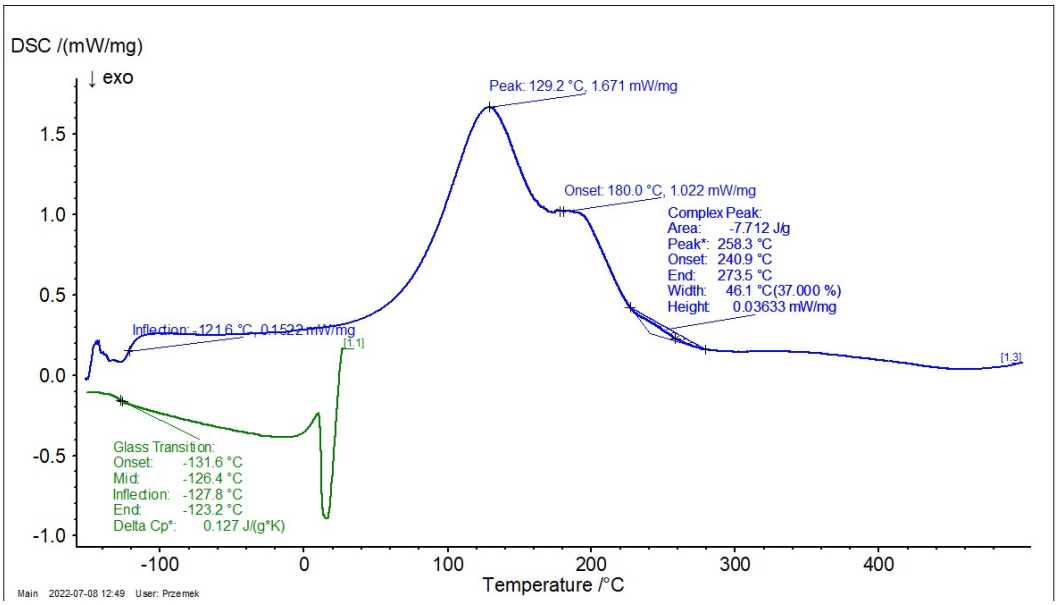

Figure S20. The DSC curve of 2-chloro-2-propen-1-ol oligomer obtained using [Ru(2-phenylpyridine)$(Cl)_2$(DMSO)(NO)] as a precatalyst.

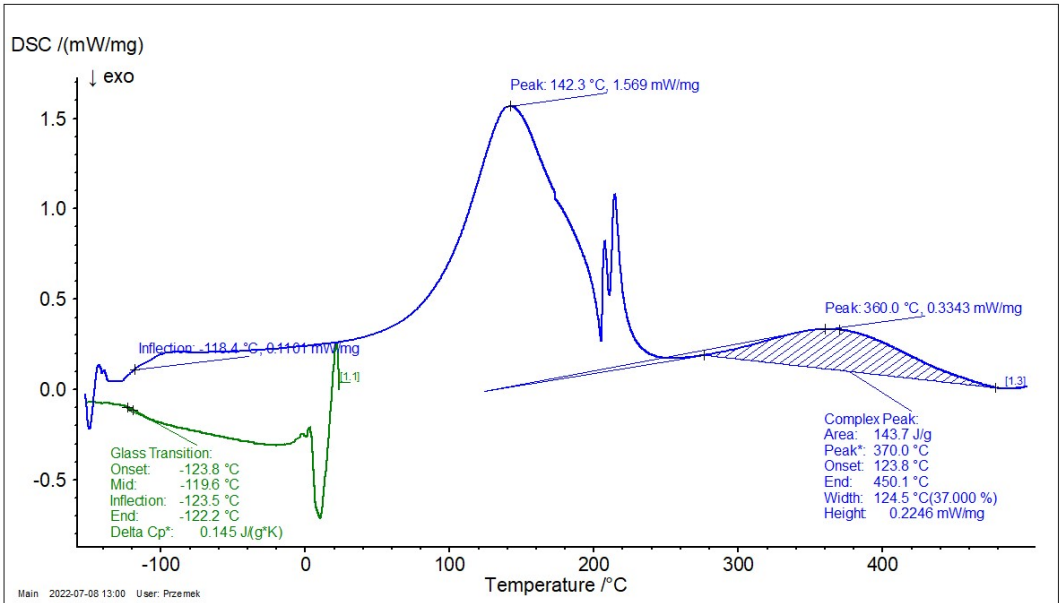

Figure S21. The DSC spectra of 3-buten-2-ol oligomer obtained using [Ru(2-phenylpyridine)$(Cl)_2$(DMSO)(NO)] as a precatalyst.

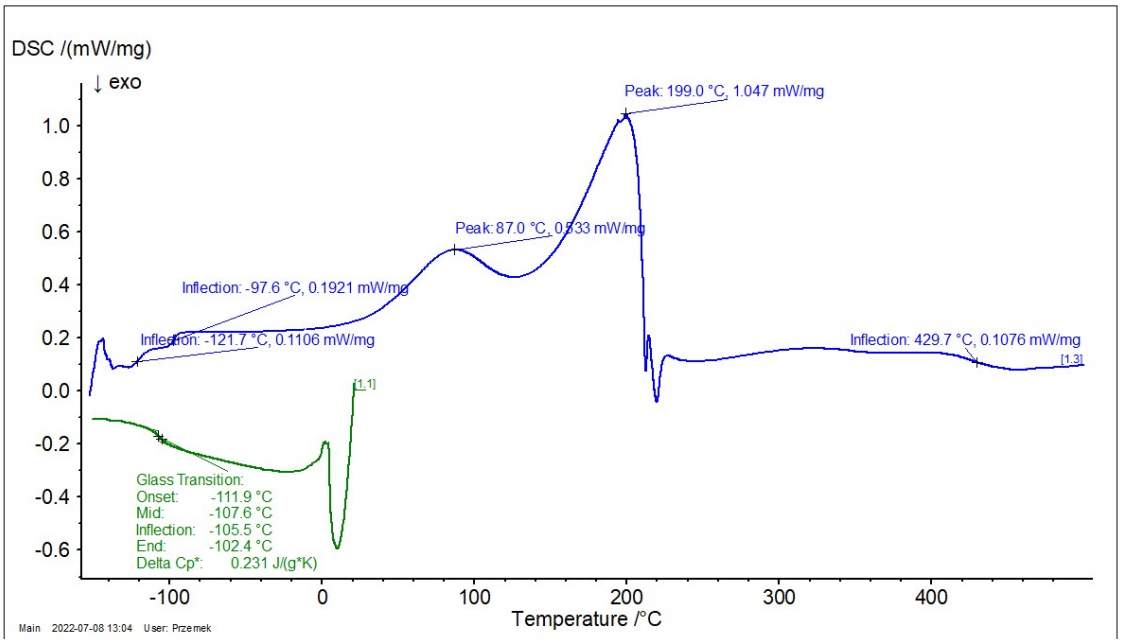

Figure S22. The DSC spectra of 2,3-dibromo-2-propen-1-ol oligomer obtained using [Ru(2-phenylpyridine)$(Cl)_2$(DMSO)(NO)] as a precatalyst.

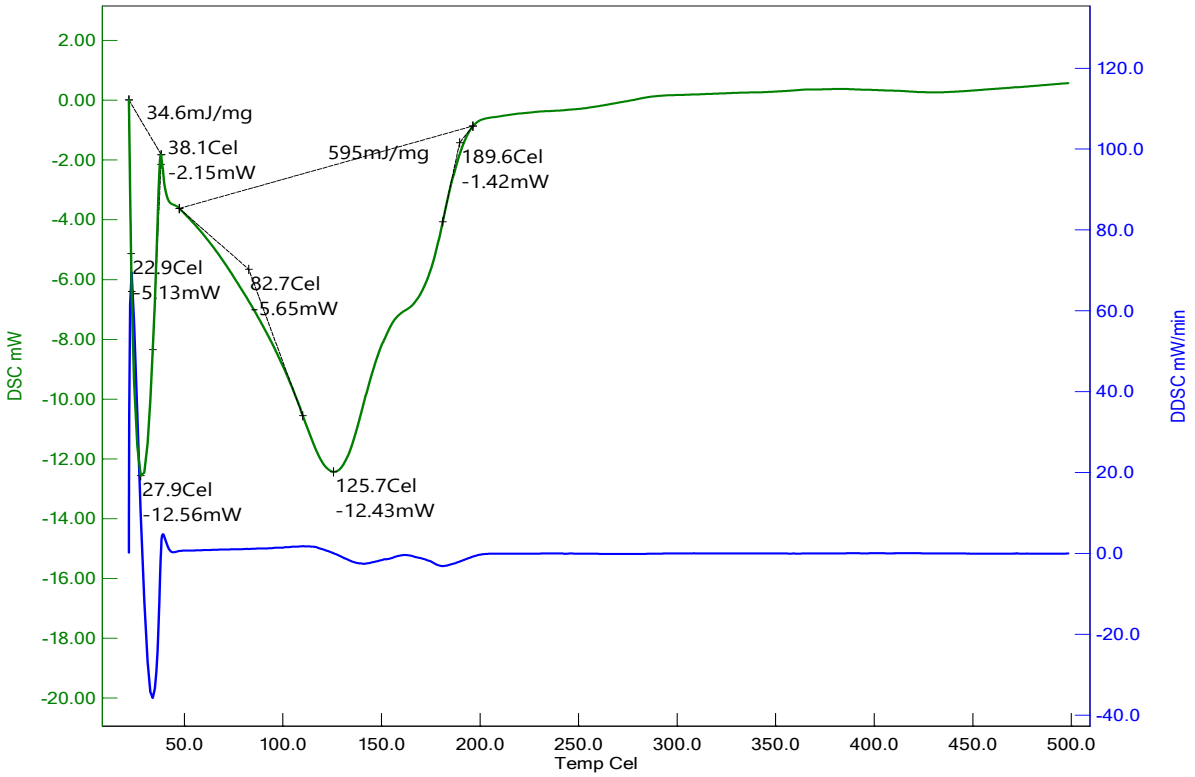

Figure S23. The DSC spectra of ethylene oligomer obtained using [Ru(2-phenylpyridine)$(Cl)_2$(DMSO)(NO)] as a precatalyst.

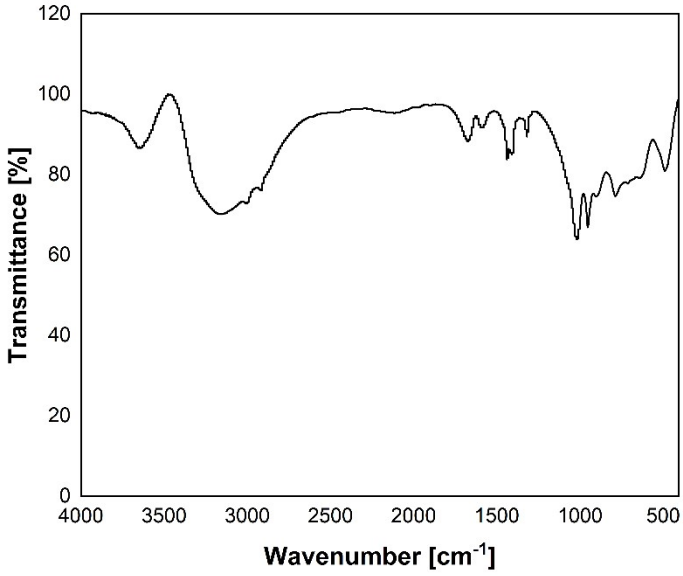

Figure S24. The FTIR spectrum of the allyl alcohol oligomer obtained using [Ru(2-phenylpyridine)$(Cl)_2$(DMSO)(NO)] as a precatalyst.

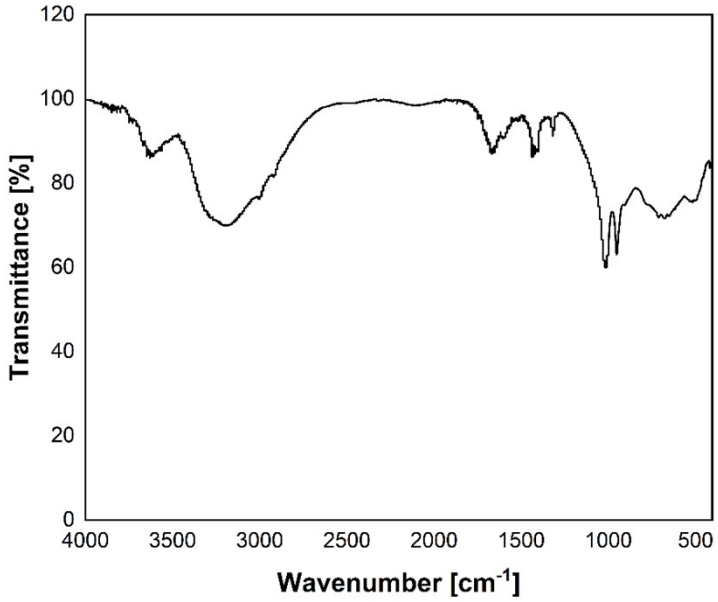

Figure S25. The FTIR spectrum of the 2-chloro-2-propen-1-ol oligomer obtained using [Ru(2-phenylpyridine)$(Cl)_2$(DMSO)(NO)] as a precatalyst.

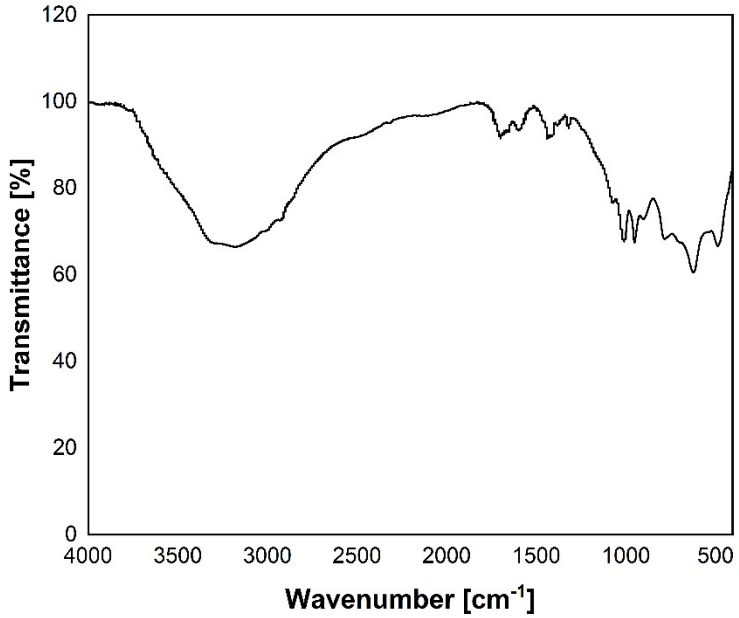

Figure S26. The FTIR spectrum of the 3-buten-2-ol oligomer obtained using [Ru(2-phenylpyridine)$(Cl)_2$(DMSO)(NO)] as a precatalyst.

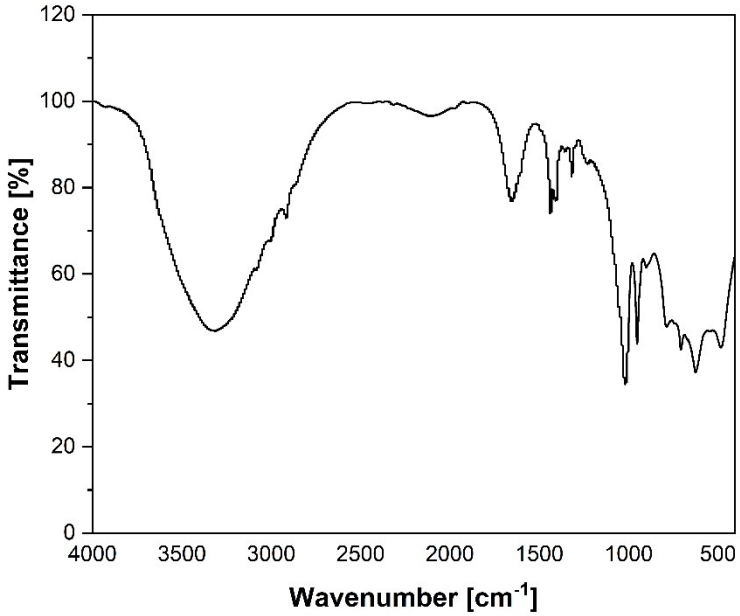

Figure S27. The FTIR spectrum of the 2,3-dibromo-2-propen-1-ol oligomer obtained using [Ru(2-phenylpyridine)$(Cl)_2$(DMSO)(NO)] as a precatalyst.

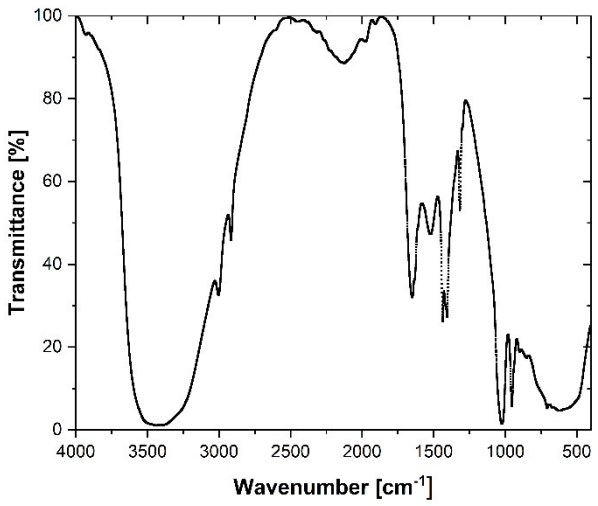

Figure S28. The FTIR spectrum of the ethylene oligomer obtained using [Ru(2-phenylpyridine)$(Cl)_2$(DMSO)(NO)] as a precatalyst.

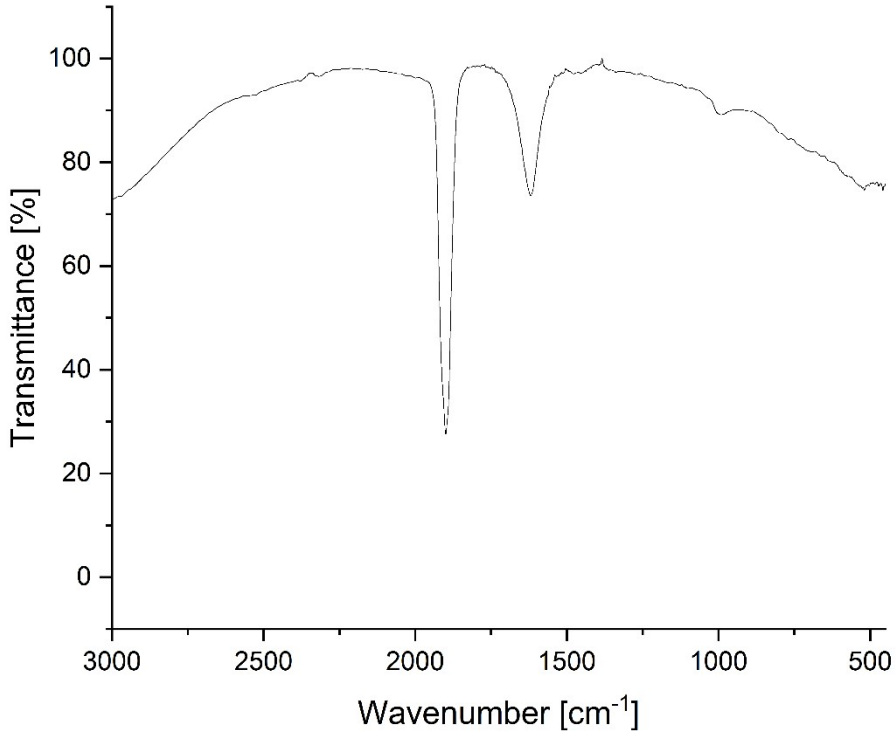

Figure S29. The FTIR spectrum of the $RuCl_3NO$ salt from BDH.

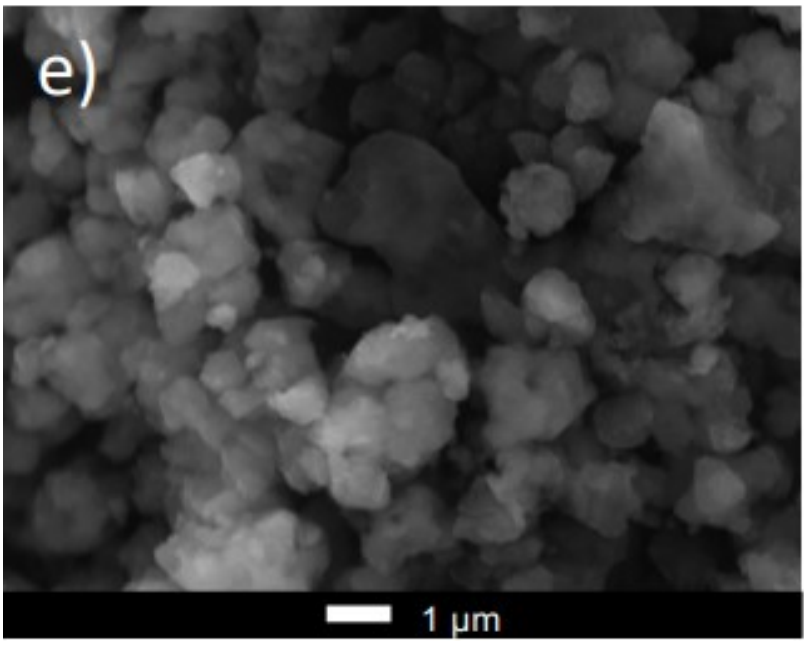

Figure S30. SEM image of the ethylene oligomer.

Table S2. Optimization of the oligomerization process of selected monomers

Monomer	Activator	Ru(III):Al	t (℃)	p (bar)	C_a[a]
		1:500	30		159.2
Allyl alcohol	MAO				
		1:1000			268.7
		1:1500			283.6
		1:2000			185.1
		1:2500			69.65
		1:1500	50		258.2
		1:1500	70		318.4
Ethylene		1:1500	30	0.3	754.7
		1:1500		0.5	755.6
		1:1500		0.8	209.7
		1:1500	50	0.5	576.5
		1:1500	70		130.5

[a]($g \bullet mmol^{-1} \bullet h^{-1} \bullet bar^{-1}$)

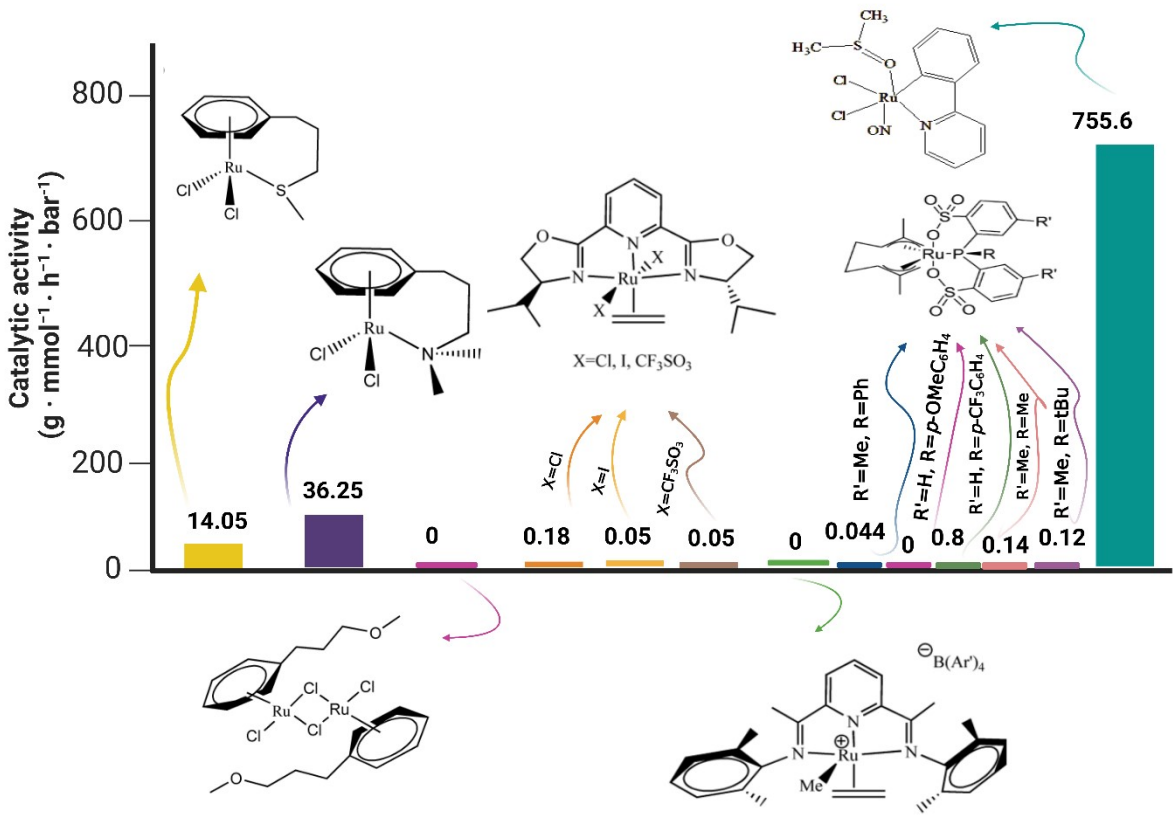

Figure S31. Comparison of the catalytic properties of ruthenium(II/III/IV) precatalysts in the oligomerization and polymerization of ethylene [21–24]. Created with BioRender.com

Proposed mechanism of coordination polymerization based on the literature.

In homogeneous catalysis, the role of MAO (methylaluminoxane) is to alkylate the precatalyst because of the exchange of ligands. The consequence is the formation of a metal-alkyl complex (Fig. S32). Then, the chloride anion is probably replaced, which correlates with the formation of the polymerization active center - the ruthenium(III) cation and the MAO anion (activation). The weakly coordinating methylaluminoxane protects the active center, so despite the small steric hindrance due to the ligands, i.e. NO and DMSO, the active center of ruthenium is not immediately poisoned. In the initiation stage, a bond is formed between the ruthenium ion and a monomer molecule, e.g. ethylene (metal-carbon bond). According to the Arlam and Cossee mechanism[25,26], propagation occurs (monomer coordination and insertion). In turn, the termination involves the elimination of β-H (or transfer to the monomer)[27–30].

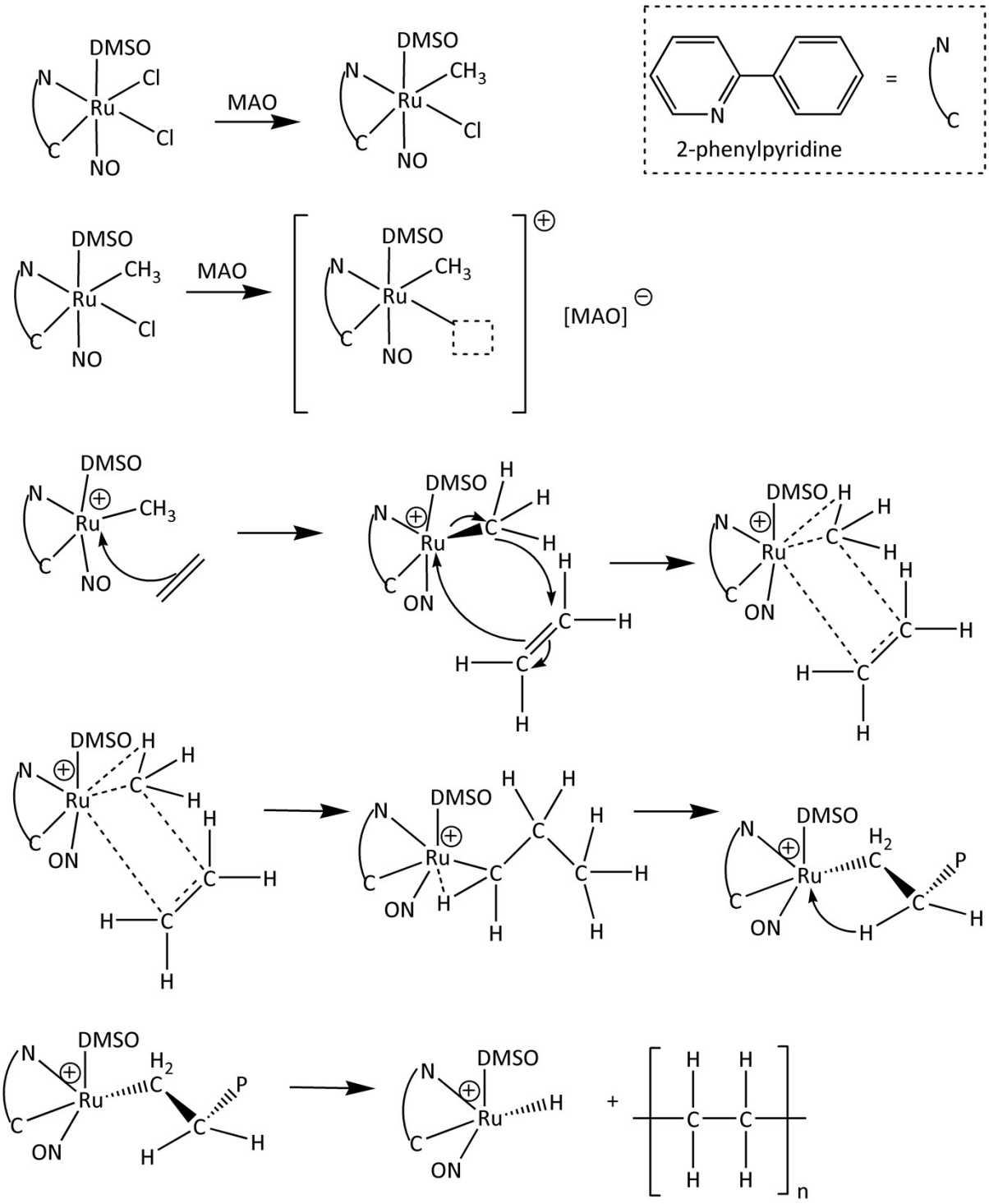

Figure S32. Proposed mechanism of coordination polymerization of ethylene using **Ru1** as a precatalyst and MAO as an activator (P = polymer and NC = 2-phenylpyridine)[25–30].

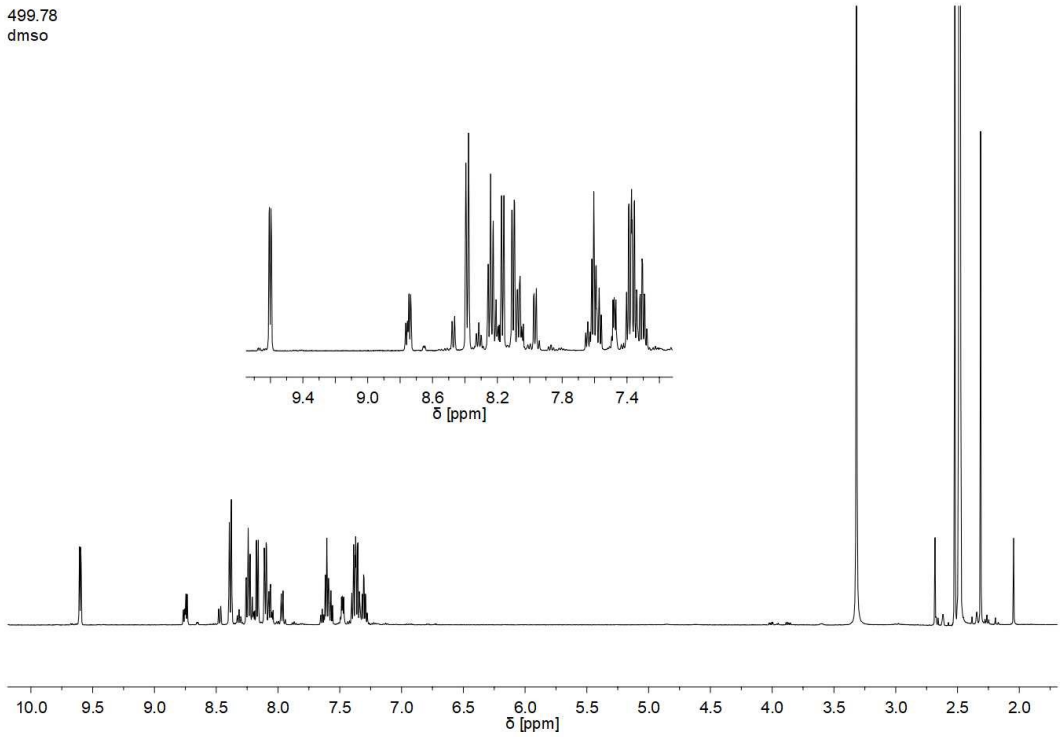

Figure S33. ^{1}H NMR spectra of **Ru1**.

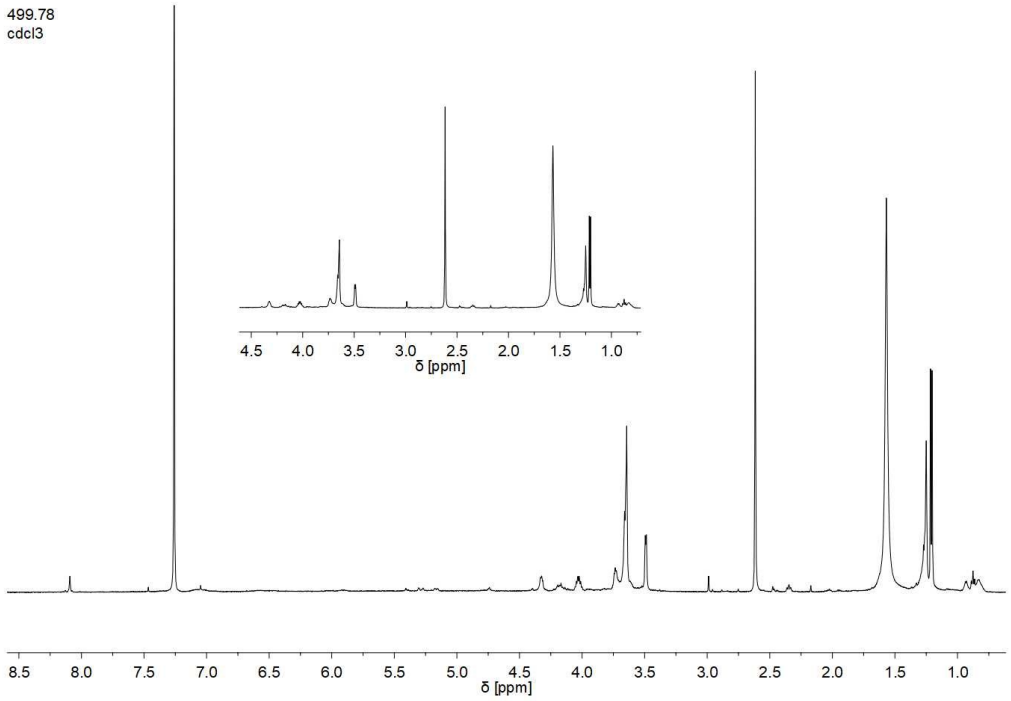

Figure S34. ^{1}H NMR spectra of allyl alcohol oligomer.

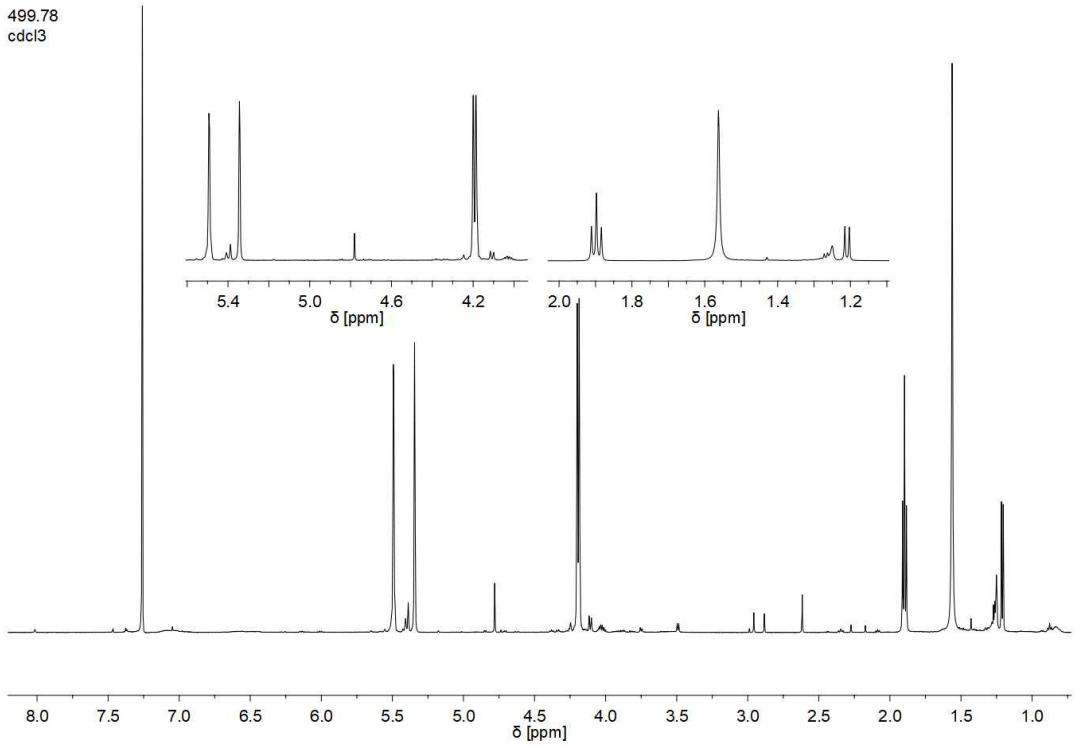

Figure S35 ^{1}H NMR spectra of 2-chloro-2-propen-1-ol oligomer.

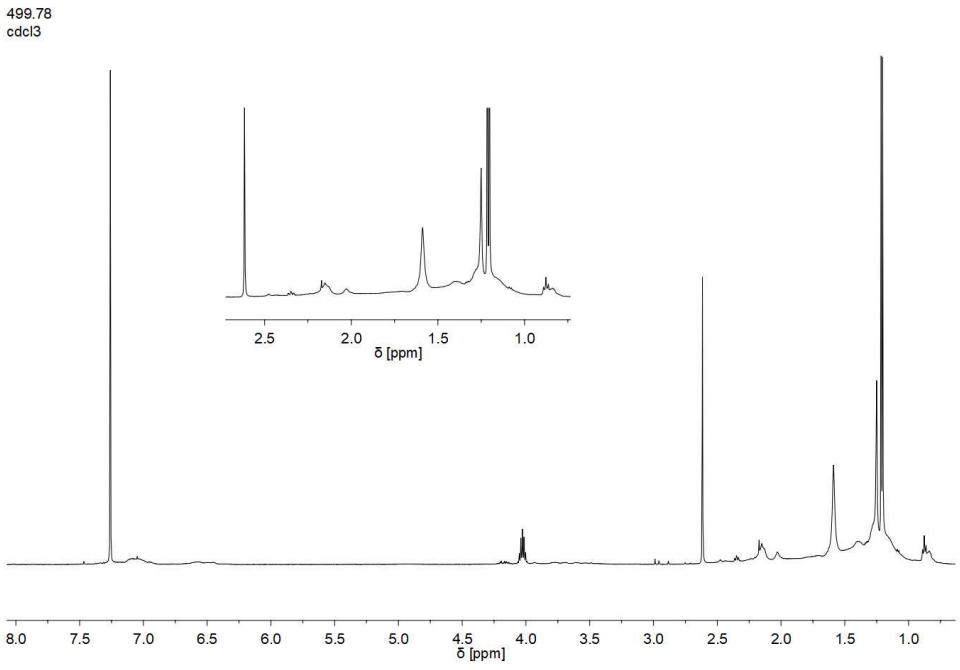

Figure S36. ^{1}H NMR spectra of 3-buten-2-ol oligomer.

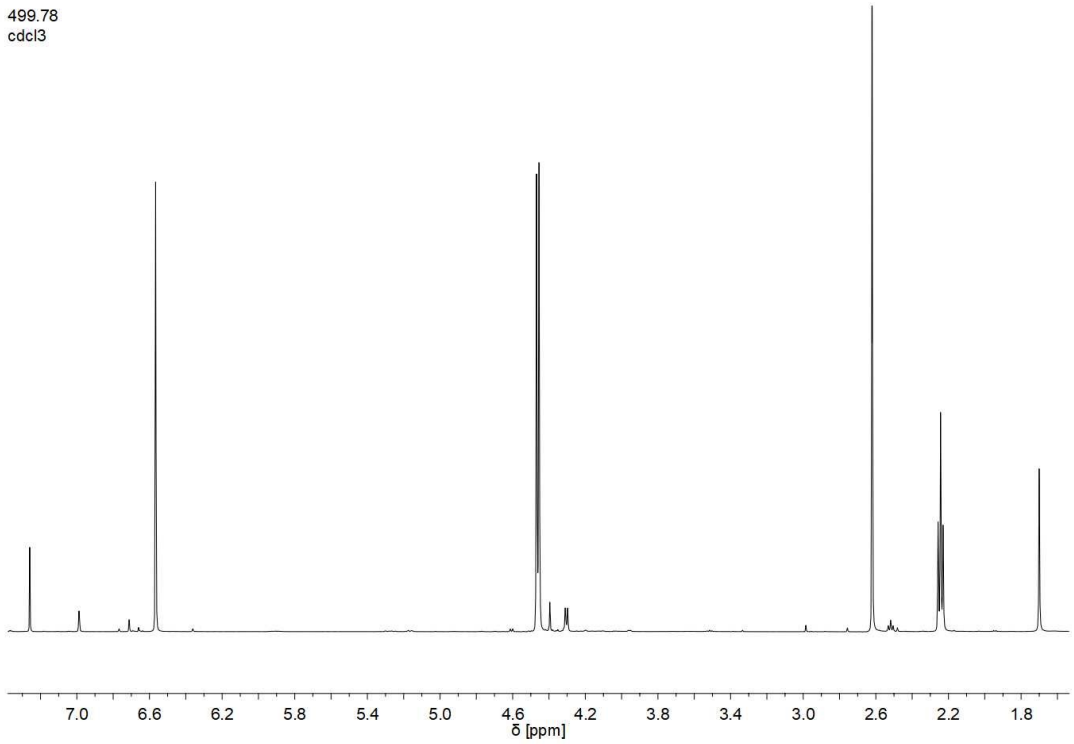

Figure S37. ^{1}H NMR spectra of 2,3-dibormo-2-propen-1-ol oligomer.

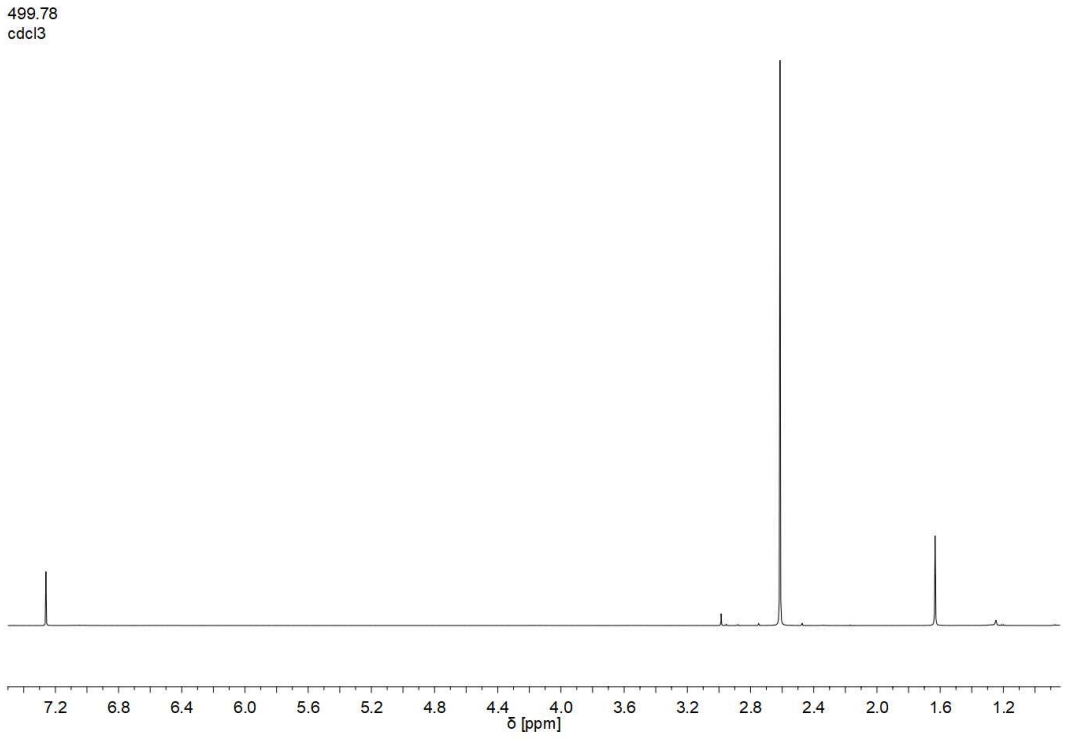

Figure S38. ^{1}H NMR spectra of ethylene oligomer.

References:

1 G. M. Sheldrick, *Acta Crystallogr C Struct Chem*, 2015, **71**, 3–8.
2 V. Petříček, M. Dušek and L. Palatinus, *Z Kristallogr Cryst Mater*, 2014, **229**, 345–352.
3 F. H. Allen, *Acta Crystallogr B*, 2002, **58**, 380–388.
4 C. R. Groom, I. J. Bruno, M. P. Lightfoot and S. C. Ward, *Acta Crystallogr B Struct Sci Cryst Eng Mater*, 2016, **72**, 171–179.
5 M. E. Frisch, G. W. Trucks, H. B. Schlegel, G. E. Scuseria, M. A. Robb, J. R. Cheeseman and D. J. Fox, .
6 P. J. Hay and Thom. H. Dunning, *J Chem Phys*, 1977, **67**, 2290–2303.
7 P. J. Hay and W. R. Wadt, *J Chem Phys*, 1985, **82**, 299–310.
8 J. P. Perdew, *Phys Rev B*, 1986, **33**, 8822–8824.
9 A. D. Becke, *Phys Rev A (Coll Park)*, 1988, **38**, 3098–3100.
10 C. Lee, W. Yang and R. G. Parr, *Phys Rev B*, 1988, **37**, 785–789.
11 S. Grimme, *J Comput Chem*, 2004, **25**, 1463–1473.
12 S. Grimme, *J Comput Chem*, 2006, **27**, 1787–1799.
13 S. Grimme, J. Antony, S. Ehrlich and H. Krieg, *J Chem Phys*, , DOI:10.1063/1.3382344.
14 S. Grimme, S. Ehrlich and L. Goerigk, *J Comput Chem*, 2011, **32**, 1456–1465.
15 S. F. Boys and F. Bernardi, *Mol Phys*, 1970, **19**, 553–566.
16 S. Simon, M. Duran and J. J. Dannenberg, *J Chem Phys*, 1996, **105**, 11024–11031.
17 R. Kamiński, K. N. Jarzembska and S. Domagała, *J Appl Crystallogr*, 2013, **46**, 540–543.
18 Y. Chen, K. N. Jarzembska, E. Trzop, L. Zhang and P. Coppens, *Chemistry – A European Journal*, 2015, **21**, 11538–11544.
19 D. Schaniel, N. Casaretto, E.-E. Bendeif, T. Woike, A. K. E. Gallien, P. Klüfers, S. E. Kutniewska, R. Kamiński, G. Bouchez, K. Boukheddaden and S. Pillet, *CrystEngComm*, 2019, **21**, 5804–5810.
20 A. A. Mikhailov, G. A. Kostin and D. Schaniel, *New Journal of Chemistry*, 2022, **46**, 12641–12650.
21 K. Nomura, W. Sidokmai and Y. Imanishi, *Bull Chem Soc Jpn*, 2000, **73**, 599–605.
22 T. Friedberger, J. W. Ziller and Z. Guan, *Organometallics*, 2014, **33**, 1913–1916.
23 M. A. Camacho-Fernandez, M. Yen, J. W. Ziller and Z. Guan, *Chem Sci*, 2013, **4**, 2902.
24 M. A. Camacho-Fernandez, J. W. Ziller and Z. Guan, *Organometallics*, 2022, **41**, 3257–3269.
25 P. COSSEE, *J Catal*, 1964, **3**, 80–88.
26 E. ARLMAN, *J Catal*, 1964, **3**, 99–104.
27 B. JAMES, *J Catal*, 1972, **27**, 442–451.
28 N. N. Dass and S. R. Sen, *Journal of Polymer Science: Polymer Chemistry Edition*, 1983, **21**, 3381–3388.
29 E. Zurek and T. Ziegler, *Prog Polym Sci*, 2004, **29**, 107–148.
30 K. P. Bryliakov, N. V Semikolenova, D. V Yudaev, V. A. Zakharov, H. H. Brintzinger, M. Ystenes, E. Rytter and E. P. Talsi, *J Organomet Chem*, 2003, **683**, 92–102.